Differential coastal uplift quantified by luminescence dating of marine terraces, central Cascadia forearc, Oregon

[1*]McKenzie, K.A., .[2]Kelsey, H.M., [3]Kirby, E., [4]Rittenour T.M., & [1]Furlong, K.P.

[1]The Pennsylvania State University, University Park, PA
[2]California State Polytechnic University, Humboldt, Arcata, CA
[3]The University of North Carolina at Chapel Hill, Chapel Hill, NC
[4]Utah State University, Logan, UT
*Present address: The University of North Carolina at Chapel Hill, Chapel Hill, NC; kmckenzie@unc.edu

Abstract

Flights of marine terraces along the coastline of the Cascadia convergent margin record long-term, sustained crustal uplift of the subduction zone upper plate. At Yaquina Bay (Newport, Oregon) differences in the elevations of previously inferred MIS 5 (5a, 5c, and 5e) marine terraces north and south of the bay imply differences in the long-term uplift rate that are attributed to displacement along the Yaquina Bay fault – a west-to-east trending fault inferred to be located within the bay. Here we present the first direct ages for the marine terrace deposits at Yaquina Bay using luminescence dating of marine terrace sands on terrace treads to quantify long-term and interval uplift rates. These new age results in combination with high-resolution topographic data, allow us to refine previous mapping of marine terraces in the vicinity of Yaquina Bay, including the recognition of a MIS 5a terrace south of Yaquina Bay. Differences in the elevations of terraces north and south of Yaquina Bay confirm relative displacement along the Yaquina Bay fault since the late Pleistocene. Our results imply differences in the long-term uplift rate relative to sea level north and south of Yaquina Bay since ca. 125 ka; south of the fault, uplift rates appear to have been relatively constant at 0.3-0.4 m/kyr, whereas north of the fault, average uplift rates were greater, 0.7-0.9 m/kyr over the past ca. 125 kyrs. Notably, terrace elevations north of the fault require variations in uplift rate through time. Uplift rates appear to have been relatively low (≤ 0.1 m/kyr) between MIS 5e and 5c but increased to rates of ~1.6 m/kyr in a ~20 kyr period between MIS 5c and MIS 5a. Subsequently, uplift rates appear to have decreased to 0.7 m/kyr during the last ~80 kyrs, but were sustained at rates approximately double that of the block south of the fault. These results require temporally variable slip along the Yaquina Bay fault since the late Pleistocene.

Key Words

Marine terraces; Luminescence dating, Geomorphology, coastal; North America; Cascadia; Forearc deformation

1. Introduction

The long-term emergence of coastlines above sea level over tens of thousands of years (encompassing many subduction earthquake cycles) has been documented along several subduction zones including the Cascadia subduction zone (Muhs et al., 1990); the Nankai subduction zone in SW Japan (Matsu'ura, 2015); the Hellenic subduction zone (Gallen et al., 2014); and Nazca plate subduction beneath South America (Saillard et al., 2011). However, models of the subduction zone earthquake cycle (e.g., Govers et al., 2017), often assume that upper-plate deformation is fully elastic and recovered over multiple earthquake cycles, negating any permanent vertical deformation. Field observations suggest otherwise; and in coastal Oregon, the highest rates of vertical displacement of late Pleistocene marine terraces relative to sea level occur adjacent to upper-plate structures, such as faults and folds (Kelsey et al., 1994). In northern Chile, the emergence of the Mejillones Peninsula has been attributed to active folding and faulting resulting from E-W directed extension across the inner portions of the forearc (Victor et al., 2011). In Peru and the Ryuku Islands of Japan, uplift of marine terraces has been attributed to the subduction of oceanic ridges (Hsu, 1992; Muhs et al., 2020). The relative role that upper-plate structures play in generating long-term coastal uplift, and how displacement along these structures is, or is not, related to deformation along the plate interface remain persistent questions in our understanding of convergent margin tectonics.

Uplifted marine terraces are one of the few geomorphic markers in landscapes that preserve records of long-term coastal uplift relative to the geoid (Bloom et al., 1974), referred to here as crustal uplift. However, eustatic variations in sea level drive variations in the formation and preservation of these features. There are two primary forms of marine terraces: (1) constructional terraces, that reflect the growth of coral reef (terrace) platforms during sea level highstands (Bloom et al., 1974); and (2) erosional terraces, that primarily form when high sea levels carve sea cliffs and form wave-cut (terrace) platforms (Bradley and Griggs, 1976). During sea-level lowstands (glacial periods) these platforms are exposed above sea level and may be preserved along coastlines when the rate of uplift exceeds subsequent sea-level rise (Bloom et al. 1974). Flights of uplifted erosional marine terraces have been identified and studied along the Cascadia subduction zone from northern California to Washington state (Griggs, 1945; Kennedy et al., 1982; Adams, 1984; West and McCrumb, 1988; Merritts and Bull, 1989; McInelly and Kelsey, 1990; Muhs et al., 1990; Kelsey, 1990; Kelsey and Bockheim, 1994; Kelsey et al., 1996; Thackary, 1998; Polenz and Kelsey, 1999; Padgett et al., 2019; Figure 1). These terraces record the effects of eustatic sea-level variations superimposed on long-term crustal uplift and upper-plate faulting and folding over numerous Cascadia subduction earthquake cycles. A suite of such marine terraces is preserved in central Cascadia in the vicinity of Yaquina Bay, Newport, Oregon (Figure 1). Here, previous work by Kelsey et al. (1996) found that these marine terraces are offset across Yaquina Bay by an inferred fault, with terraces north of the bay at higher elevations relative to their respective counterparts south of the bay. This interpretation was based on age assignments determined by the correlation of the degree of soil development among terraces at Yaquina Bay and terraces in southern Oregon that had been dated using ^{230}Th/^{234}U dating of coral or amino acid racemization methods (Muhs et al., 1990; Kennedy et al., 1982; Kelsey et al., 1996; and, more recently by Muhs et al., 2006). Kelsey et al. (1996) correlated the youngest three terraces in this region to sea-level highstands at 80 ka, 105 ka, and 125 ka corresponding to marine oxygen isotope stages (MIS) 5a, 5c, and 5e respectively.

Kelsey et al. (1996) report that two faults that offset the inferred 80 ka platform in the vicinity of Newport (Yaquina Bay fault, Yaquina Head fault) have the same sense of offset and general trend as faults mapped by Snavely et al. (1976) in underlying Paleogene sediment. Kelsey et al. (1996) suggest that the late-Pleistocene-active faults may have trends inherited from these earlier structures.

In this paper we evaluate the age assignments of Kelsey et al. (1996) based on two new data sets. Recent availability of 1 m (nominal grid size) resolution digital topography derived from Lidar data allows us to use a surface classification model (SCM) (Bowles and Cowgill, 2012) to refine the locations and elevations of the mapped marine terrace surfaces and terrace shoreline angles in this region; locations that were previously delineated using aerial photographs followed by field mapping (Kelsey et al., 1996). Combining this high-resolution topographic mapping with optically stimulated luminescence (OSL) dating of quartz and infrared stimulated luminescence (IRSL) dating of potassium (K) feldspar within marine terrace sands, allows us to assign paleo-sea level highstand ages to the marine terraces exposed at Yaquina Bay. We use these new data to evaluate long-term (and interval-specific) crustal uplift at Yaquina Bay and evaluate the history of displacement along the Yaquina Bay fault. Finally, we compare our results to previous estimates of long-term terrace uplift rates and present-day geodetic uplift rates along the Cascadia margin.

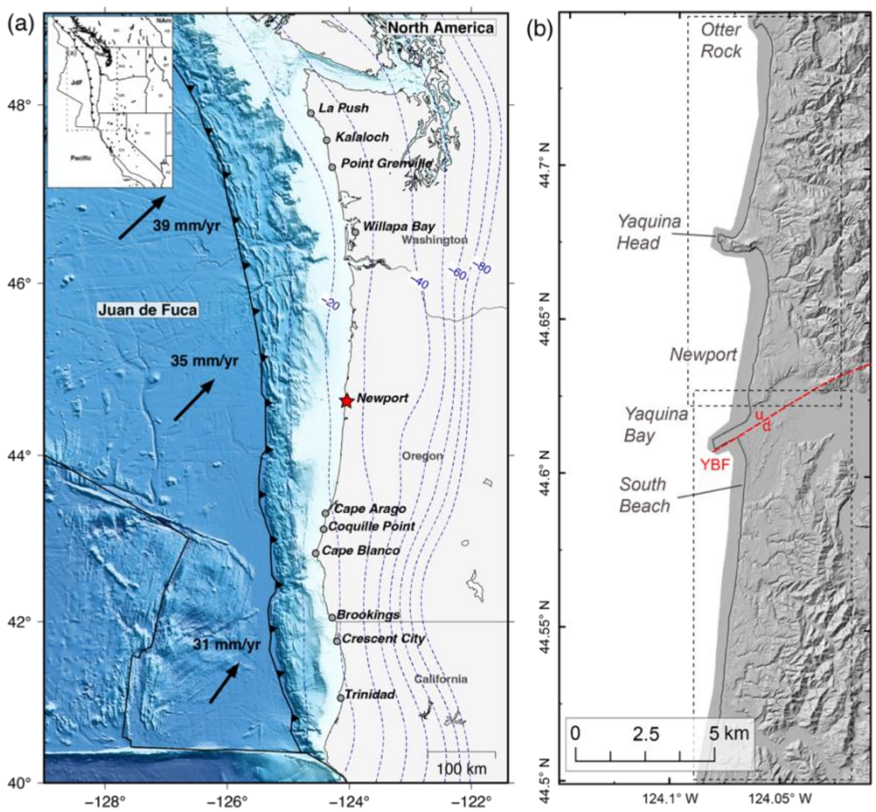

Figure 1: (a) Map of the Cascadia subduction zone showing the locations along the coastline of previous marine terrace studies in Oregon and California (Griggs, 1945; Kennedy et al., 1982; Adams, 1984; West and McCrumb, 1988; Merritts and Bull, 1989; McInelly and Kelsey, 1990; Muhs et al., 1990; Kelsey, 1990; Kelsey and Bockheim, 1994; Kelsey et al., 1996; Thackary, 1998; Polenz and Kelsey, 1999; Padgett et al., 2019). Newport is highlighted by the red star. The dashed blue lines are the Slab2 subduction zone slab depth contours (Hayes, 2018). (b) Topographic hillshade map of the study region in the vicinity of Newport, Oregon. The dashed boxes show the regions north and south of Yaquina Bay shown in subsequent figures (2, 3(b) and (c), 5(b) and (c), and 6). The dashed red line is the inferred position of the Yaquina Bay fault (YBF) (Kelsey et al., 1996) - u = upthrown block; d = downthrown block.

2. Background

2.1. The Cascadia subduction zone

The Cascadia subduction zone stretches from northern California to British Columbia (Figure 1) and is characterized by the oblique (NE-directed) subduction of the Juan de Fuca (Gorda south of 43 °N) plate beneath North America. Although there have been no significant recent earthquakes along the Cascadia plate boundary, paleo-seismic data from both estuarine and submarine environments, historic records of tsunami inundation in Japan, and Native American oral traditions provide evidence for previous large megathrust events (e.g. Atwater, 1987; Atwater et al., 1991; Nelson et al., 1995; Satake et al., 1996; Atwater and Hemphill-Haley, 1997; Yamaguchi, 1997; Clague et al., 2000; Kelsey et al., 2002; Witter et al., 2003; Ludwin et al., 2005; Nelson et al., 2008; Hawkes et al., 2011; Goldfinger et al., 2012). These records provide evidence for the most recent 1700 CE ~Mw 9 earthquake which is inferred to have ruptured the entire length of the subduction zone (Wang et al., 2013), and smaller ~Mw 8+ earthquakes that are proposed to have previously ruptured distinct segments on the subduction plate interface (Goldfinger et al., 2012; Kelsey et al., 2005; Witter et al., 2012).

In Cascadia, several sequences of late Pleistocene marine terraces record a ~100,000-to-200,000-year history of coastal uplift, and in some locations deformation of these platforms records Quaternary faulting and folding (e.g., Kelsey et al., 1994). This record likely spans hundreds of subduction earthquake cycles over which standard elastic models would produce zero net vertical motion (e.g., Govers et al., 2017). Although such models produce no net uplift or subsidence, the uplift and preservation of marine terraces, coral atolls, and river terraces, as well as faulting and folding along subduction zones imply that some fraction of subduction earthquake-cycle deformation is retained permanently in the geologic record (e.g., Melnick et al., 2006; Meltzner et al., 2006; Ramírez-Herrera et al., 2018; Saillard et al., 2017). Additionally, the Cascadia subduction zone is characterized by an emergent forearc mountain range, that appears to have sustained rock uplift and erosion since at least Miocene time (VanLaningham et al., 2006; Kobor and Roering, 2004; McNeill et al., 2000). A comparison of long-term uplift rates with numerical models of subduction coupling for the Cascadia subduction zone suggest that as much as ~25-50 % of the inter-earthquake deformation along the central Oregon coastline can become permanent upper-plate deformation (McKenzie et al., 2022).

However, displacement histories along upper-plate structures are poorly understood along much of the margin, and yet are necessary for a better understanding of the relationship between upper-plate structures and permanent strain above subduction zones.

2.2 Characterization of Marine Terraces at Yaquina Bay

Yaquina Bay is situated along the coast at Newport in central Oregon approximately ~100 km east of the subduction trench and ~25 km above the plate interface (Figure 1) (Hayes, 2018). In this region six marine terrace platforms have been identified above present-day sea level (Kelsey et al., 1996). The three youngest, lowest elevation terraces at Yaquina Bay have been previously assigned ages of 80 ka, 105 ka, and 125 ka, corresponding to MIS 5a, 5c and 5e respectively (Kelsey et al., 1996). These age correlations were based on the degree of soil development (Kelsey et al., 1996) of dated terraces along the southern Oregon coast (Muhs et al., 1990; Kennedy et al., 1982). Older, higher elevation terraces are also observed at Yaquina Bay, the lowest of which is assumed to be associated with the next oldest paleo-sea level highstand at ~200 ka (Kelsey et al., 1996). However, this terrace and the two older terraces are highly dissected by stream networks and are poorly preserved in this region (Kelsey et al., 1996; this study).

Here we analyze the extent and distribution of the terraces preserved at Yaquina Bay, focusing on the three lowest, inferred to be MIS 5a, 5c and 5e terraces (Kelsey et al., 1996). We combine high-resolution elevation models with age determinations for these terraces using OSL dating of quartz and IRSL dating of K-feldspar within marine terrace sands. This allows us to test these previous age assignments, and in doing so, quantitively assess the long-term crustal uplift rates and the potential for active upper-plate faulting in the region.

3. Geomorphic characterization of terraces

3.1 Terrace Surface Mapping

We use a 1 m horizontal resolution Lidar-derived digital elevation model (DEM) accessed through the Oregon Department of Geology and Mineral Industries (DOGAMI) website (https://www.oregongeology.org, collected by the Oregon Lidar Consortium) to map marine terrace surfaces and estimate the location of paleoshorelines associated with each mapped terrace. We used the method of Bowles and Cowgill (2012) to create a surface classification model (SCM) that identifies areas of low topographic slope and roughness inferred to represent terrace surfaces. Several authors have used this method (Bowles and Cowgill, 2012) to map marine terrace surfaces from DEMs (e.g., Racano et al., 2020; Padgett et al., 2019). Following these previous studies, first we generated a slope map from the Lidar-derived DEM (Figure 2) and determined the standard deviation of the slope (defined as terrain roughness (Frankel and Dolan, 2007)), using a 3x3 cell rectangular moving window. Marine terraces typically slope 1-6° (Bowles and Cowgill, 2012) oceanward but slope values up to 15° have been observed (Bradley and Griggs, 1976). Thus, we only used slope values ≤ 15° in our analysis. Regions of high topographic roughness may reflect artifacts of low-resolution regions within the DEM and thus we removed roughness values greater than 1 standard deviation from the mean roughness (> 4). The SCM was then determined by normalizing and combining the slope and roughness values (weighted equally) using (1) (Bowles and Cowgill, 2012):

$$SCM = 0.5\left(\frac{slope}{15}\right) + 0.5\left(\frac{std(slope)}{4}\right)$$
$$0 < slope < 15 \qquad (1)$$
$$0 < std(slope) < 4$$

We manually digitized marine terrace surfaces by outlining low SCM regions (close to 0) overlain on a hillshade map generated from the 1 m resolution Lidar DEM (Figure S1). Outlining terrace surfaces manually allowed us to avoid false identification of terrace surfaces in low SCM regions that instead represent roads, the present-day beach and bay area adjacent to Newport, large river channels, and the airport south of Yaquina Bay. We constructed a frequency distribution of elevations within the outlined terrace surfaces to identify peaks in elevation ranges that can be used to differentiate terrace surfaces (Figure S2; Bowles and Cowgill, 2012).

A (paleo)shoreline angle is a quasi-linear feature that defines the intersection between a marine wave-cut platform and corresponding (paleo)sea cliff that is used as a marker for mean sea level at the time the wave-cut platform was formed (Lajoie, 1986). At Yaquina Bay, the paleoshoreline angles are buried beneath cover sediment and thus we defined the surface expression of a paleoshoreline angle as a quasi-linear feature sub-parallel to the present-day shoreline that lies at the base of a steep slope and separates mapped terrace surfaces within different elevation ranges (Figures 2, 3). In regions where the paleoshoreline could not be defined (i.e., because of dense stream networks and/or human-made features) we interpolated the paleoshoreline location between regions where the feature was better preserved. We chose not to connect the paleoshorelines across regions cut by large west-east channels that have dissected the landscape.

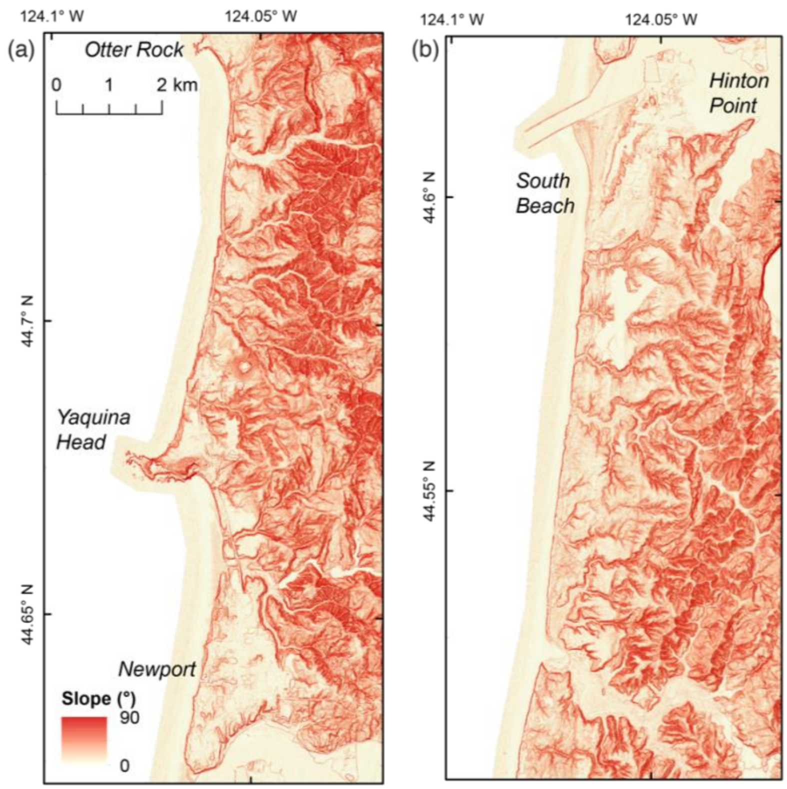

Figure 2: Slope maps for the Yaquina Bay/Newport region. (a) North of Yaquina Bay, (b) South of Yaquina Bay. The locations of (a) and (b) are shown in Figure 1(b).

3.2 Mapping Results

We identified three distinct terrace platforms north of Yaquina Bay and five distinct terrace platforms south of Yaquina Bay. The lower elevation (younger) terraces are well defined compared to the higher elevation (older) terraces that have been significantly dissected and eroded over time (Figures 3, 4 and 5). We analyzed marine terraces on the north and south side of Yaquina Bay separately to test previous work suggesting that these terraces have been offset vertically across Yaquina Bay (Kelsey et al., 1996). In our description of the terraces below, we do not assume a terrace age *a priori*, and instead define the terraces as surfaces 1n, 2n, 3n (north of Yaquina Bay), 1s, 2s, 3s, 4s and 5s (south of Yaquina Bay), with surfaces 1n and 1s being the lowest elevation terraces at both sides of the bay. Figure 3 shows the elevation of the mapped surfaces and paleoshorelines and Figure 4 shows shoreline perpendicular elevation profiles through the three lowest elevation terrace surfaces at either side of Yaquina Bay.

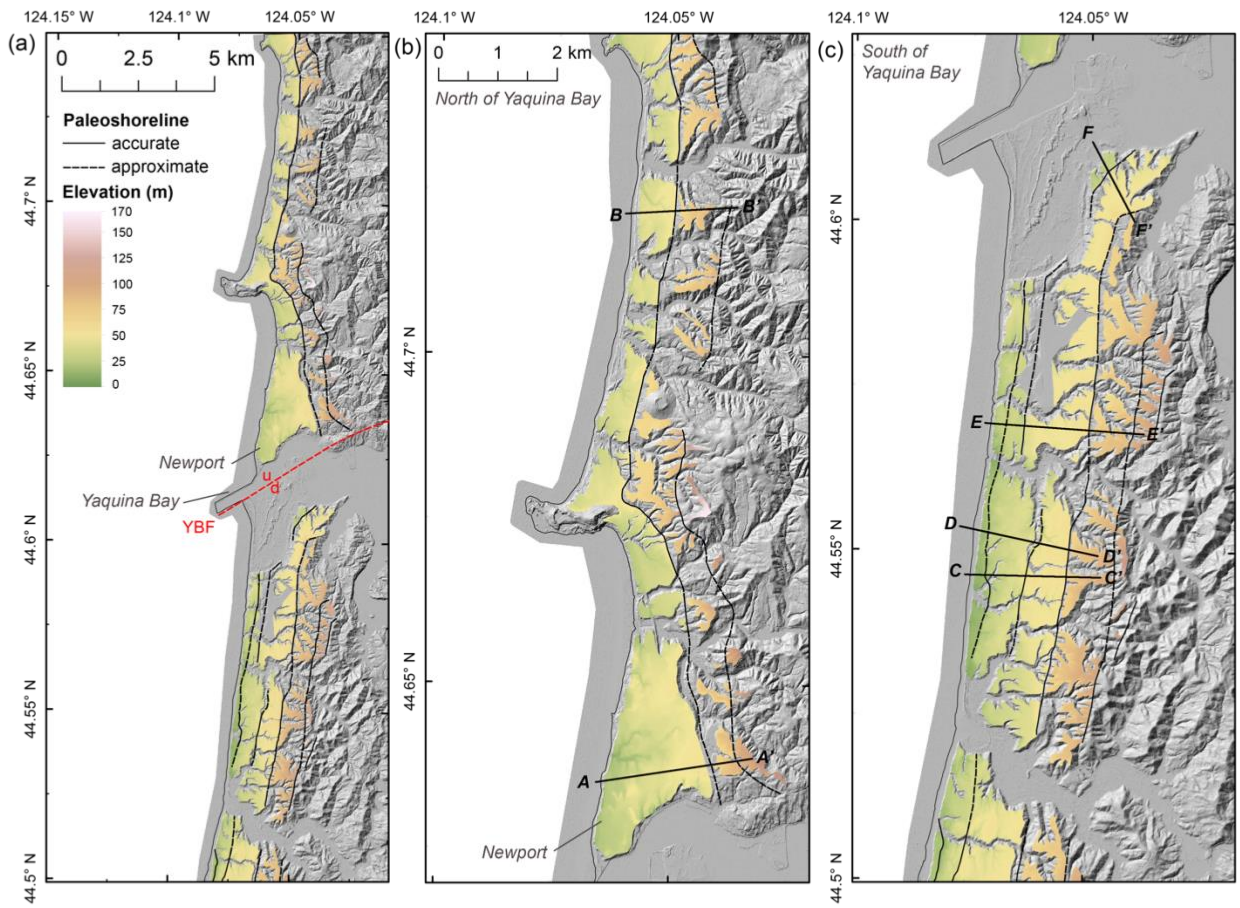

Figure 3: Lidar hillshade maps overlain by polygons of terrace surfaces (determined from SCM analysis) and estimated locations of terrace paleoshorelines. (a) Map of full Yaquina Bay region. The dashed red line is the inferred position of the Yaquina Bay fault (YBF) (Kelsey et al., 1996) - u = upthrown block; d = downthrown block. (b) Map north of Yaquina Bay. (c) Map south of Yaquina Bay. The location of elevation profiles (A-A’, B-B’, C-C’, D-D’, E-E’, and F-F’) shown in Figure 4 are shown in (b) and (c).

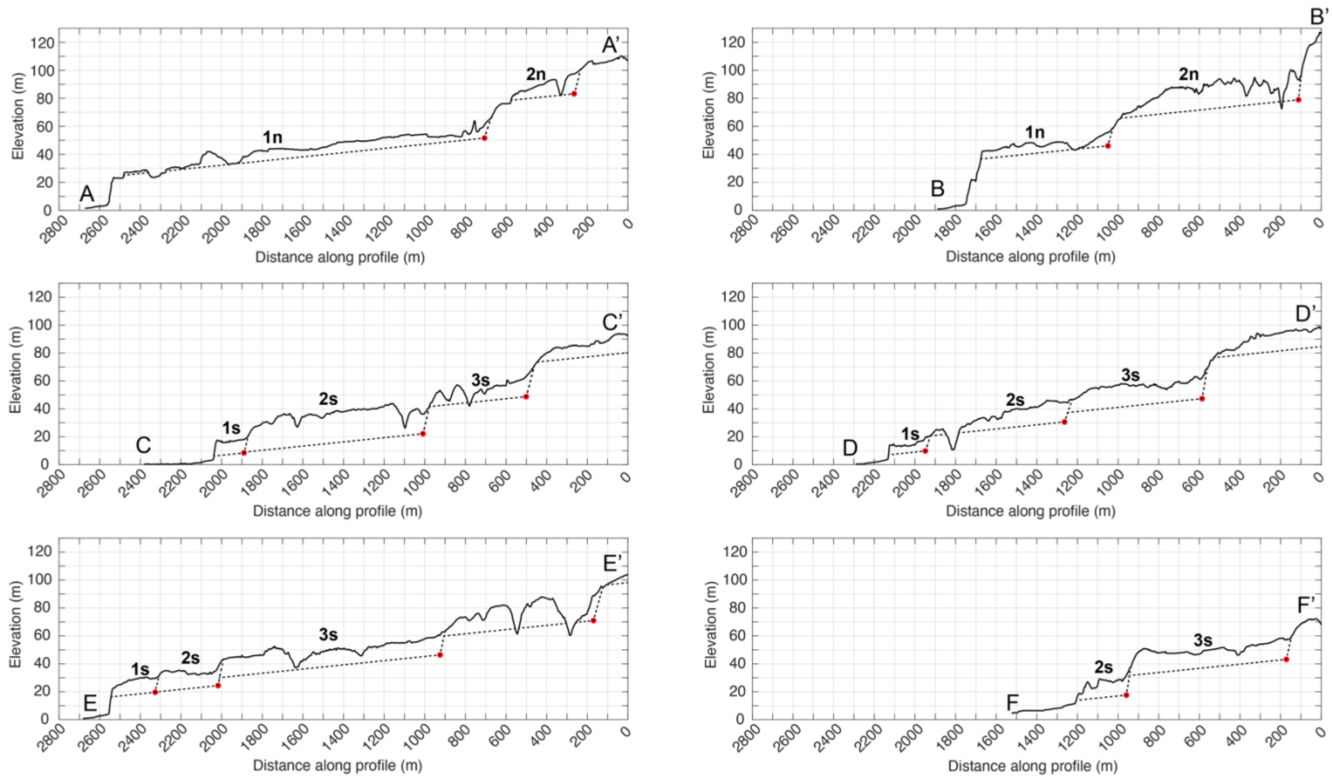

Figure 4: Vertically exaggerated shoreline perpendicular elevation profiles (west to east) through the marine terraces mapped north and south of Yaquina Bay. The location of each profile line is shown in Figures 3(b) and (c). Profiles A-A' and B-B' are locations north of Yaquina Bay and profiles C-C', D-D', E-E' and F-F' are location south of Yaquina Bay. Terraces are labeled based on their relative elevation: 1n, 2n, 3n (north of Yaquina Bay), 1s, 2s, and 3s (south of Yaquina Bay). The red dots show the approximate location of the paleo-shoreline angle for each terrace, below an assigned average cover sediment thickness (Table 2). The black dashed lines show our interpretation of where the terrace platforms and paleo-sea cliffs are beneath the present-day surface and terrace cover sediment. The methodology for estimating the paleo-shoreline angle is described in section 5.1.1.

3.2.1 North of Yaquina Bay

We identified three terrace surfaces north of Yaquina Bay, with the most distinctive terrace being the lowest terrace (surface 1n). This terrace is separated from the next highest terrace by a steep N-S trending escarpment – representing its corresponding paleo-sea cliff – north of the town of Newport (Figure 2). Surface 1n is ~30-50 m in elevation above present-day sea level (Figures 3, 4, S2) and ranges in width from ~2000 m at Newport to ~600-700 m north of 44.65 °N (Figure 3). Just north of Yaquina Bay, within Newport itself, we approximated the location of the paleoshoreline between surface 1n and surface 2n by changes in elevation because dissection of the landscape by rivers and human-made features such as road networks and buildings made identifying any slope changes here difficult. Surface 2n and its respective paleoshoreline location were most easily identified near to Yaquina Head and Otter Rock (Figure 1(b)) at the northern end of our study region (Figures 2, 3 and 4). Surface 2n is ~500-900 m in width and ~70-90 m in elevation north of Yaquina Bay. Surface 3n is ~100-120 m in elevation. Identification of surface 3n was only possible in certain locations where erosion and channel dissection were minimal. Due to this slope degradation, we could not confidently determine the location of the surface 3n paleoshoreline from the Lidar mapping or the range of widths for surface 3n north of Yaquina Bay.

3.2.2 South of Yaquina Bay

We mapped five distinct terrace surfaces south of Yaquina Bay (surfaces 1s-5s). The lowest-most surface, surface 1s, is relatively narrow (100-200 m where exposed), ranges in elevation from ~10-20 m, and dips shallowly (0.1-0.2 °) to the south. In many locations the paleoshoreline separating surfaces 1s and 2s was approximated based on subtle slope changes in the Lidar-derived DEM (Figures 2, 3 and 4). Surface 1s cannot be identified by a distinctive peak in the frequency distribution plot of terrace surface elevations (Figure S2), likely because of its patchy exposure compared to the higher elevation surfaces (Figures 3, 4 and 5). Surface 2s ranges in elevation from ~20 – 40 m and ranges in width from ~200 – 900 m, with the narrowest exposure being closest to Yaquina Bay, where surface 1s is not exposed (Figure 3 and 4(f)). The paleoshoreline separating surfaces 2s and 3s is most distinct near to profiles C-C' and E-E' (Figures 2, 4(c) and 4(d)), but in many cases it was approximated based on changes in elevation and subtle slope changes identified from shoreline perpendicular profiles. Surfaces 2s and 3s were differentiated by two prominent peaks at ~35 m and ~50 m in the frequency distribution plot of surface elevations (Figure S2). There are several N-S striking stream channels most apparent near to profiles C-C' and D-D' (Figures 2, 3), that appear to separate these two surface elevation bands and are sub-parallel to the paleoshoreline separating surfaces 2s and 3s. This may suggest that when this paleoshoreline was exposed above sea level, preexisting stream channels preferentially flowing along the base of the sea cliff, maintained course and obscured any evidence of a distinct slope break associated with a paleoshoreline. Surface 3s ranges in elevation from ~40-60 m and ranges in width from ~500-1100 m. The paleoshoreline between surfaces 3s and 4s was identified at the base of a prominent linear (high slope) feature representing a paleo-sea cliff (Figure 2). Surface 4s is ~80-90 m in elevation (Figures 3, 4) and ranges in width from ~500-1000 m. Surface 5s is > 100 m in elevation and is extensively eroded by stream networks (Figures 2 and 3).

3.2.3 Comparison to Previous Mapping

North of Yaquina Bay, our mapping results are consistent with the previous mapping of Kelsey et al. (1996), with minor differences in the location/elevation of the paleoshorelines and the extent of the mapped surfaces. We were able to refine these features with the high-resolution Lidar data. South of Yaquina Bay, we identified three terrace surfaces between the present-day shoreline and surface 4s, in contrast with the previous field mapping (Kelsey et al., 1996) that only mapped two surfaces. The identification of the two lowest terraces (surfaces 1s and 2s) south of Yaquina Bay was based on subtle topographic features observed in the high-resolution Lidar data, including slope breaks observed discontinuously from north to south (Figure 4), N-S trending (shoreline parallel) stream networks (Figure 3), and the frequency distribution of elevations of the mapped surfaces (Figure S2). The mapping of higher platforms remains the same. We now present luminescence ages for these terrace platforms to determine the age-elevation distribution of the terraces mapped north and south of Yaquina Bay.

4. Luminescence Age Determinations: Methods and Results

4.1 Overview

We use luminescence dating of terrace sands in the vicinity of Yaquina Bay to compare to the previous terrace age estimates at Yaquina Bay (Kelsey et al., 1996), and develop new uplift rate estimates (Figures 3, 4 and 5). At the time of initial terrace mapping (Kelsey et al., 1996), luminescence techniques were not a feasible approach to determine marine terrace age. The ages reported here represent the first direct ages for these coastal localities and the first OSL and IRSL ages for any marine terraces along the Cascadia margin. The applicability of luminescence techniques to dating marine terraces heralds promise for more extensive dating of marine terrace sand in mid-latitude settings where traditional radiometric dating techniques have been limited by the lack of suitable sample material (Jacobs, 2008; Morel et al., 2022; Muhs et al., 2022).

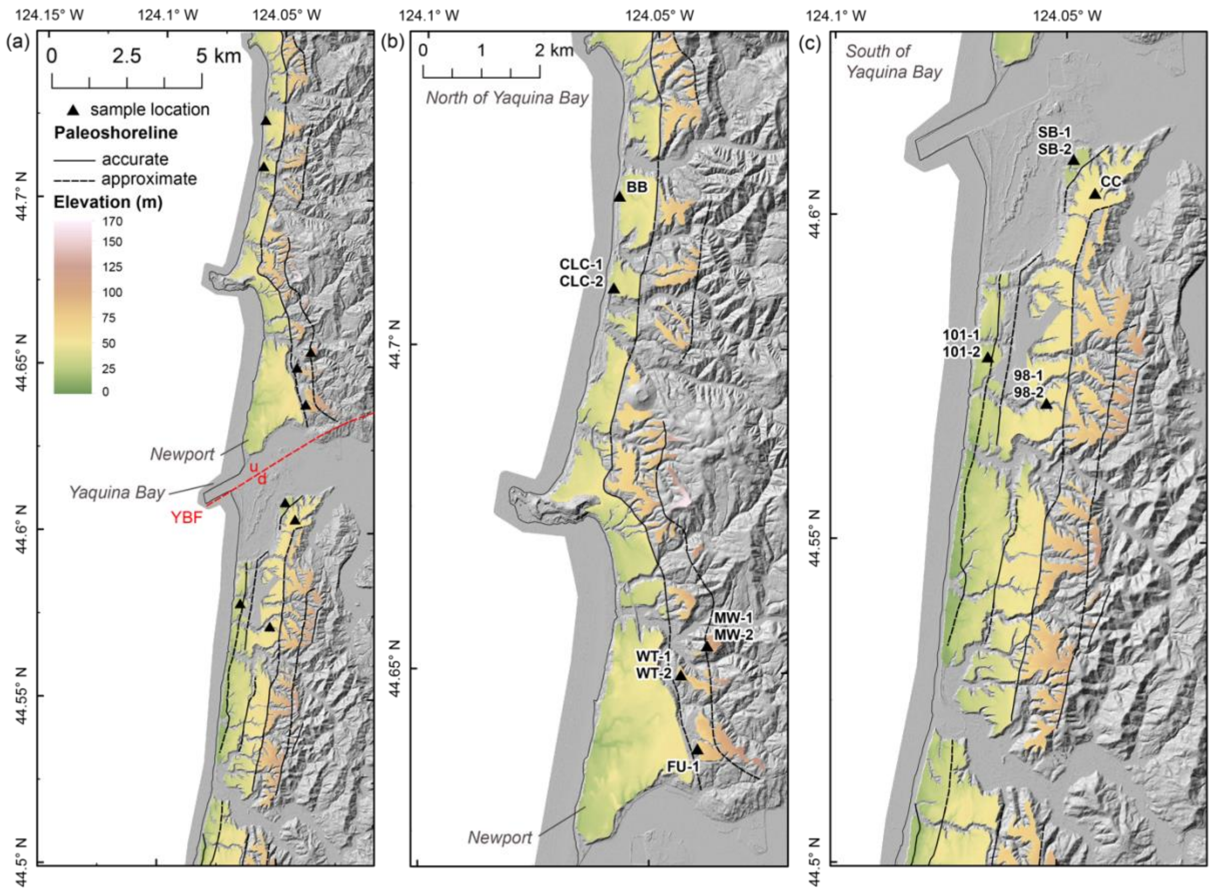

Figure 5: Lidar hillshade maps overlain by polygons of terrace surfaces and estimated locations of terrace paleoshorelines. The location of the luminescence sample sites are shown by black triangles and labeled in (b) and (c). The red dashed line in (a) shows the approximate location of the Yaquina Bay fault.

4.2 Sample Collection

We use OSL of quartz and IRSL of K-feldspar to date sand deposited above the mapped terrace platforms on either side of Yaquina Bay. Sites that were sampled for OSL had the following characteristics: we selected massive sand that in most instances had evidence of undisturbed sedimentary structure in the form of planar beds or cross beds. The presence of undisturbed sedimentary structure minimized the possibility of bioturbation. We sampled sand as close to the underlying platform as possible to ensure that we were sampling nearshore or beach sand and not any overlying fluvial sand if present. We did not observe any evidence of fluvial features such as cross cutting channels at any of our sample locations. Samples were collected in a metallic tube (1.5” diameter, 8” length) hammered horizontally into a fresh surface exposure and sealed from light upon collection. One sample (FU-1) was taken vertically to avoid observed bioturbation at the site. Fifteen total samples were collected, distributed across nine field sites. These include duplicates collected at six sites and single samples collected at three sites (BB, CC and FU-1). Samples were collected from the three lowest elevation terraces north of Yaquina Bay (previously assigned as terraces that formed during MIS 5a, 5c, and 5e (Kelsey et al., 1996)), and the three lowest elevation terraces south of Yaquina Bay (previously mapped as two terraces and assigned ages of MIS 5c and 5e (Kelsey et al., 1996)). Samples 101-1 and 101-2 are from a single sample site located along highway 101 (Figure 5) within the region previously mapped as the MIS 5c terrace by Kelsey et al. (1996). Sample nomenclature is as follows: Abbreviated location of sample-sample number (upper sample (U) or lower sample (L)), e.g., CLC-1(U). Photographs of samples sites and a table of their locations are in the supplemental material (Figures S3 and S4, Table S1).

4.3 Sample Processing and Age Determinations

Samples were processed and analyzed at the Utah State University Luminescence Laboratory. Samples were opened in dim amber light and wet sieved to 150-250 µm, then treated with hydrochloric acid and peroxide to remove carbonates and organic material. The K-feldspar fraction was isolated for IRSL dating, using sodium polytungstate separation at 2.58 g/cm^3. The quartz fraction was separated for OSL dating using mineral separation at 2.72 g/cm^3, and subsequently underwent hydrochloric acid and hydrofluoric acid treatments to etch and purify the quartz. The presence of residual feldspar within quartz samples (i.e., the purity of the quartz) was determined using infrared-stimulation.

4.3.1 Dose Rate Determination

The concentration of U, Th, K and Rb in terrace deposits was measured by ICP-MS and ICP-AES. Dose rate calculations were then determined using conversion factors from Guérin et al. (2011). For feldspar analyses, the internal grain beta dose rate was calculated assuming 12.5%

K (Huntley and Baril, 1997) and 400 ppm Rb (Huntley and Hancock, 2001) attenuated to grain size using Mejdahl (1979). An ‘a-value’ (efficiency factor) of 0.09 ± 0.01 (Rees-Jones, 1995) was used to determine the alpha contribution to the IRSL dose rate. Radio-elemental chemistry (U, Th, K content), sediment moisture and cosmic contribution were taken into account for dose rate determinations (Aitken and Xie, 1990; Aitken, 1998). To avoid applying sediment moisture values that appear to have greater precision and accuracy than we could obtain from the one-time water content samples, we rounded moisture content values to the nearest 5%, based on field point measurements and field capacity constraints (following Nelson and Rittenour, 2015). For OSL and IRSL dating, the sample depth, elevation and location (longitude and latitude) were used to determine the contribution of cosmic radiation to the dose rate following Prescott and Hutton (1994).

4.3.2 Luminescence Measurements

Due to continual reworking of sediment in nearshore and beach environments, the luminescence signal of sediment in these environments has been shown to be reset quickly, e.g., young (< 100 yr) coastal and marine sediments have been shown to give accurate luminescence ages (Madsen and Murray, 2009). We used the single-aliquot regenerative-dose (SAR) procedures for OSL dating of quartz sand (Murray and Wintle, 2000, 2003; Wintle and Murray, 2006), and for IRSL dating of K-feldspar measured at 50°C (Wallinga et al. 2000). Each sample was irradiated at five different dose levels: below, at, above the equivalent dose (D_E), zero dose, and a repeated dose to test for recuperation of the signal and sensitivity correction. The resulting dose-response curve results were fit with a saturating exponential curve. Fading corrections (loss of the signal with time) were calculated for IRSL ages using the linear-fit method of Auclair et al. (2003) and the age correction method of Huntley and Lamothe (2001). OSL and IRSL ages were determined using the Central Age Model (CAM) of Galbraith and Roberts (2012).

4.4 OSL and IRSL Results

Table 1 contains the age results for the OSL analyses. Table 1 also contains IRSL results for two samples whose (fading-corrected) ages are consistent with the OSL age for the same sample. Further results including dose rate information and equivalent dose distributions can be found in the supplemental material (Table S2, Figure S5).

Samples BB, CLC-2, 101-1 and 101-2 returned ages (within the analytical uncertainty) consistent with MIS 5a (84 ka). 101-1 and 101-2 are located south of Yaquina Bay, within surface 1s (Figures 5 and 6) and therefore imply that the MIS 5a terrace is exposed south of the bay. CLC-1 has an anomalously young age of 63 ± 7 ka compared to MIS 5a, which may indicate that this sample contains younger sand, suggesting a later aeolian input or mixing of younger sediment through bioturbation and/or soil processes. Samples SB-1, SB-2, WT-1 and WT-2 have ages that can be associated with MIS 5c (106 ka). The OSL and IRSL ages (113 ± 14 ka and 114 ± 11 ka respectively) of sample FU-1 overlap with MIS 5c (106 ka) and MIS 5e (125 ka) within uncertainty, however we assign this sample to MIS 5c based on its geomorphic association with the map-surface 2n (Figures 5 and 6). Samples 98-1, 98-2, MW-1, MW-2, and CC (OSL age) can be attributed to an MIS 5e (125 ka) terrace. The IRSL age for sample CC (112 ± 11 ka), similar to FU-1, overlaps with MIS 5c and MIS 5e. We assign sample CC to MIS 5e based on its location within surface 3s (Figures 5 and 6).

4.5 Discussion of Luminescence Results

The luminescence age results presented in Table 1 allow us to assign the lowest terrace south of Yaquina Bay, recognized through our terrace surface classification, to be a MIS 5a terrace (Figure 6). We evaluated the marine soils data presented in Kelsey et al. (1996) in light of our new terrace interpretation south of the bay. Soil samples LC2 and TH2 that are located within our mapped surface 1s, near luminescence samples sites 101-1 and 101-2, have a thinner Bt horizon thickness (0-30 cm) compared to sample NS2 (Bt thickness of 65 cm) that is located within our mapped surface 2s, near to luminescence samples site SB-1 and SB-2 (Kelsey et al., 1996). These observations suggest samples LC2 and TH2 are from a younger terrace than sample NS2, and thus are consistent with our luminescence results (Table 1) and Lidar mapping (Figure 5). Our mapping of the (inferred) MIS 5e terrace at Hinton Point, OR (south of Yaquina Bay) agrees with previous age assignments and mapping by Kelsey et al. (1996) and the age determined by Kennedy et al. (1982) through the correlation of amino acid racemization methods. Thus, our results allow us to correlate the mapped terraces across Yaquina Bay and evaluate previous correlation of Kelsey et al. (1996). These correlations imply differential displacement of terrace surfaces since the late Pleistocene along the Yaquina Bay fault.

Table 1: OSL and IRSL age results

Sample ID	Mapped Surface	Method	Depth from outcrop surface (m)	No. of aliquots†	Dose rate (Gy/kyr)	Equivalent Dose†† ± 2σ (Gy/kyr)	Age ± 1σ (ka)	Assigned marine isotope stage (MIS)*
North of Yaquina Bay								
BB	1n	OSL	2.55	8(14)	1.68 ± 0.07	138.92 ± 42.12	83 ± 14	MIS 5a
CLC-1(U)	1n	OSL	1.8	11(21)	1.81 ± 0.07	113.93 ± 15.41	63 ± 7	MIS 5a
CLC-2(L)	1n	OSL	2.25	12(23)	1.76 ± 0.07	153.80 ± 21.59	88 ± 9	MIS 5a
WT-1(U)	2n	OSL	2.2	10(13)	1.73 ± 0.08	180.83 ± 27.33	110 ± 12	MIS 5c
WT-2(L)	2n	OSL	2.8	10(21)	1.62 ± 0.08	169.54 ± 26.03	105 ± 12	MIS 5c
FU-1	2n	OSL	2.1	11(14)	1.76 ± 0.07	198.77 ± 35.56	113 ± 14	MIS 5c
FU-1	**2n**	**IRSL††** **(4.9 ± 1.6)**	**2.1**	**17(19)**	**2.85 ± 0.12**	**194.99 ± 20.03**	**114 ± 11**	**MIS 5c**
MW-1(U)	3n	OSL	4	14(23)	1.73 ± 0.07	211.29 ± 39.52	122 ± 15	MIS 5e
MW-2(L)	3n	OSL	4.55	10(21)	1.54 ± 0.06	198.36 ± 28.00	129 ± 14	MIS 5e
South of Yaquina Bay								
101-1(U)	1s	OSL	2.5	11(23)	1.82 ± 0.08	156.44 ± 20.26	86 ± 9	MIS 5a
101-2(L)	1s	OSL	3.5	11(26)	1.61 ± 0.07	139.91 ± 9.13	87 ± 8	MIS 5a
SB-1(L)	2s	OSL	8.5	13(30)	1.35 ± 0.05	149.16 ± 24.11	110 ± 13	MIS 5c
SB-2(U)	2s	OSL	7	14(19)	1.55 ± 0.06	163.83 ± 42.84	106 ± 16	MIS 5c
98-1(U)	3s	OSL	1.8	13(18)	1.73 ± 0.07	216.83 ± 28.53	126 ± 13	MIS 5e
98-2(L)	3s	OSL	2.1	12(20)	1.79 ± 0.07	224.21 ± 28.81	126 ± 13	MIS 5e
CC	3s	OSL	1	12(20)	1.79 ± 0.07	211.03 ± 21.73	118 ± 11	MIS 5e
CC	**3s**	**IRSL††** **(3.6 ± 0.8)**	**1**	**15(16)**	**2.75 ± 0.11**	**215.53 ± 25.00**	**112 ± 11**	**MIS 5e**

*MIS 5a = 84 ka; MIS 5c = 106 ka; MIS 5e = 125 ka.

†Age analysis using the single aliquot regeneration-dose procedure of Murray and Wintle (2000) on 1-mm small-aliquots of quartz sand (OSL 150-250 μm) or 1-mm feldspar sand following Wallinga et al. (2000) at 50°C (IRSL 50-250 μm). Number of aliquots used in age calculation and number of aliquots analyzed in parentheses

††Equivalent does (D_E) calculated using the Central Age Model (CAM) of Galbraith and Roberts (2012)

‡IRSL age on each aliquot corrected for fading (fading rate g2days, %/decade) following the method by Auclair et al. (2003) and correction model of Huntley and Lamothe (2001)

5. Long-term rock uplift from terrace elevations

To calculate the long-term uplift rate of marine terraces relative to modern sea level we need to know or estimate the elevation of the paleoshoreline angle (a marker for mean sea level at the time of terrace formation) at present and the paleo-sea level highstand elevation relative to present-day sea level.

5.1 Paleoshoreline Angle and Paleo-Sea Level Values

5.1.1 Paleoshoreline Angle

The elevation of the paleoshoreline angles for each terrace beneath the present-day surface can be determined by subtracting the cover sediment thickness from the elevation of the mapped location of the paleoshoreline (Figure 3, 4). Due to the dense vegetation cover and land-use within the study region, we observed the wave-cut platform in few places and could not directly measure the cover sediment thickness across the entire study region. Following a similar methodology as Padgett et al. (2019), we assume that the MIS 5 terrace platforms preserved at Yaquina Bay experienced similar coastal processes to regions in southern Oregon and northern California and are overlain by a similar thickness of cover sediment. We estimated the average cover sediment thickness for each platform by taking the average of the maximum and minimum sediment thicknesses for the MIS 5 terraces mapped in northern California, and southern and central Oregon (Kelsey et al. 1996; Padgett et al. (2019), and references therein) (Table 2). Based on the elevation of two exposures of the MIS 5c wave-cut platform relative to the elevation of the observed cover sediment, we estimated a cover sediment thickness of 4-6 m above the MIS 5c wave-cut platform. These values are towards the lower end of the cover sediment thickness estimates for the MIS 5c terrace along the Oregon coastline (Table 2). We note that the wide range of cover sediment thickness estimates (Table 2) introduces errors (up to 8 m) in the estimates of the paleoshoreline angle elevation, and we include these errors in our uplift rate calculations. We used the field measured paleoshoreline height given in Kelsey et al. (1996) for the MIS 5e terrace north of Yaquina Bay, since we were unable to locate the MIS 5e paleoshoreline from the Lidar. We then assumed an average platform slope of 15 m/km (Bradley and Griggs, 1976) for each terrace platform beneath this defined cover sediment thickness (Figure 4), to estimate the location of the terrace platform beneath the present-day topography.

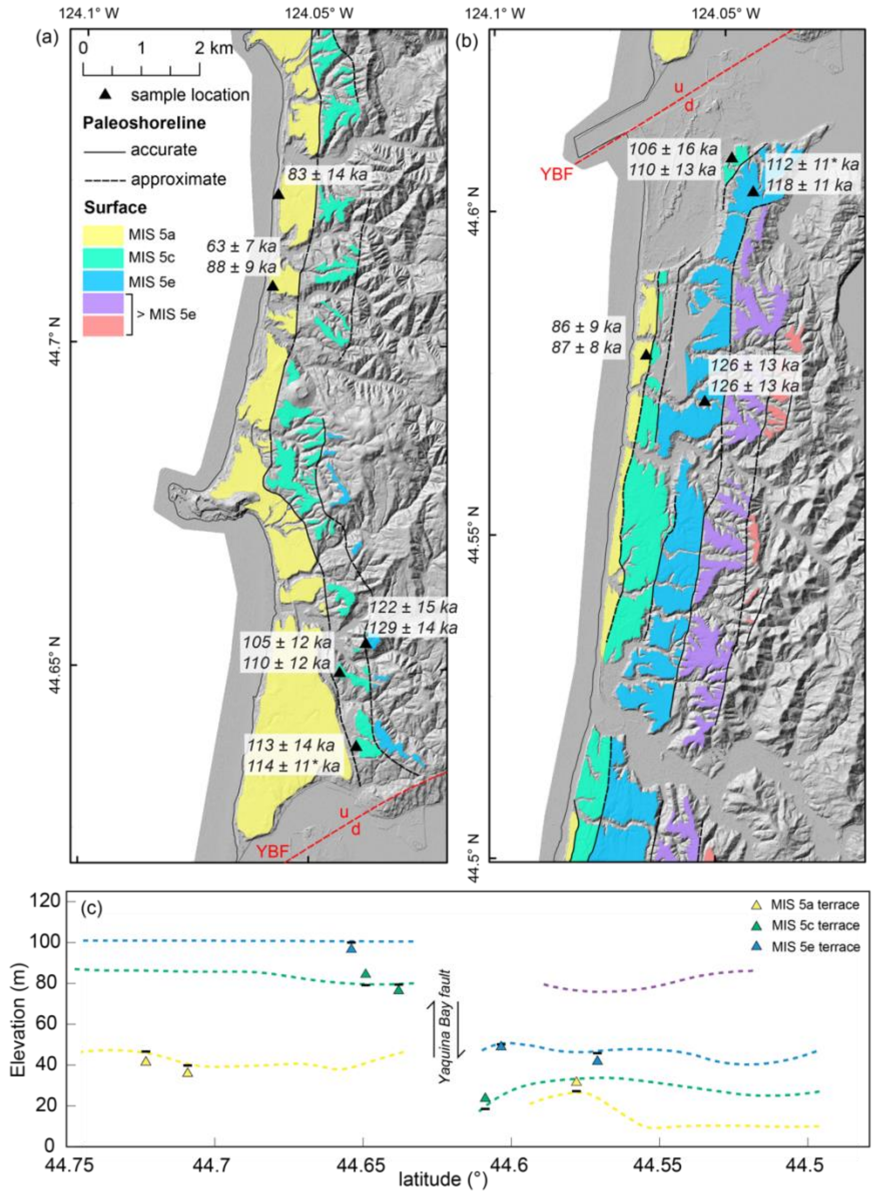

Figure 6: Terrace surface map showing the luminescence ages at each sample site. (a) North of Yaquina Bay. (b) South of Yaquina Bay. Surfaces are color-coded and assigned a marine isotope stage based on the luminescence age determinations: yellow = MIS 5a; green = MIS 5c; blue = MIS 5e; purple and red are undated but are inferred to be older than MIS 5e based on their elevation. (c) Age-Latitude plot showing the elevation of samples with latitude, colored by their assigned surface age. Dashed lines are the approximated elevations of the paleo-shoreline angles, colored by the respective surface they correspond to. Black bars are the locations of the paleo-shoreline angles at the latitude of the sample sites (shown as triangles). *indicates IRSL age in (a) and (b).

Table 2: Table of terrace geomorphic characteristics (paleoshoreline height and cover sediment thickness).

Terrace	North of Yaquina Bay	South of Yaquina Bay	Cover Sediment Thickness† (m)		
	Paleoshoreline height (m)	Paleoshoreline height (m)	Average minimum	Average maximum	Subtracted thickness
MIS 5a	38-52	8-22	5.2	13.9	10 ± 5
MIS 5c	78-94	17-35	6.6	21.8	14 ± 8
MIS 5e	100-105*	37-55	6.8	22.0	14 ± 8

*Measured from the mapped paleo-shoreline elevations (Figure 8) in Kelsey et al. (1996)

†Determined from the averages given in Padgett et al. (2019) for southern Oregon and northern California (references therein) with the incorporation of cover sediment thicknesses for terraces in central Oregon given in Kelsey et al. (1996)

N/A = not mapped in this location

5.1.2 Paleo-Sea Level Values

Various studies have determined local and global (eustatic) paleo-sea level highstand elevations for MIS 5e, MIS 5c and MIS 5a (e.g., Chappell and Shackleton, 1986; Muhs et al., 1990; Muhs, 1992; Muhs et al., 1992; Muhs et al., 2012; Creveling et al., 2015; Simms et al. 2016; Creveling et al., 2017; Table S3). These estimates are derived from sites inferred to be subject to limited Earth deformation (e.g., Chappell and Shackleton, 1986, Muhs et al., 1992) or corrected for changes in surface elevation associated with glacial isostatic adjustment (GIA) (e.g., Creveling et al. 2015, 2017; Simms et al., 2016). Many highstand estimates derived from field observations are from far-field localities (relative to North America) and so do not include local GIA effects that are particularly important at high latitudes. In contrast, local highstand values determined using GIA-models depend on a variety of factors, including the ice extent, both during the interstadial period and during preceding colder periods, the location of the peripheral bulge relative to the coastline, and the upper and lower mantle viscosity structure (Creveling et al. 2015, 2017). In several locations (including at Newport, Oregon), local GIA-corrected highstand elevations for MIS 5a, 5c and 5e conflict with highstand estimates from sea level models that do not incorporate GIA corrections (Creveling et al., 2017; Creveling et al. 2015; Simms et al., 2016; Muhs et al. 2021).

We test whether the long-term average and interval-specific uplift rates vary significantly depending on the highstand elevation chosen for MIS 5c and 5a (Table S4). We test far-field estimates of paleo sea-level highstands, estimates for North America (not corrected for GIA), and local GIA-corrected modeled values (Table S4). We find that although there are minor differences in the uplift rate estimates during specific time intervals when different MIS 5c and 5a highstand values are used, the trends from one time interval to another do not change. Specifically, by employing these sensitivity tests, we find that even by minimizing the difference in highstand elevation between MIS 5e, 5c, and 5a (Figure S4), terrace elevations still require an increase in uplift rate in the block north of Yaquina Bay (Figure 7), implying significant differential displacement across the Yaquina Bay fault post-MIS 5c (Figure 6; Table S4). For the remainder of this manuscript, we present uplift rates based on local GIA-corrected highstand values of -9 m ± 5 m and -15 m ± 5 m for MIS 5c and MIS 5a respectively (Creveling et al., 2017, to the nearest meter), and +9.5 m ± 8.5 m for MIS 5e (Creveling et al., 2015; S. Thompson, *personal communication*). We assign an uncertainty of ± 5 m to the MIS 5a and MIS 5c values, comparable to the uncertainties for local MIS 5c and MIS 5a estimates (Creveling et al., 2017).

5.2 Uplift Rate Calculation

We calculated the average long-term uplift rate north and south of Yaquina Bay for each marine terrace by dividing the uplift amount (the difference between the modern elevation of the paleoshoreline angle and the paleo-sea level highstand elevation relative to modern sea level) by the assigned paleo-highstand age at MIS 5a (84 ka), 5c (106 ka) and 5e (125 ka) (Shackleton and Opdyke, 1973; Chappell and Shackleton, 1986; Simms et al., 2016), yielding an estimate of the average uplift rate from each paleo-sea level highstand to the present. We then calculated interval uplift rates between each paleo-sea level highstand, (e.g., the uplift rate for 19 kyrs between 125 ka (MIS 5e) and 106 ka (MIS 5c)) for each adjacent terrace pair north and south of the bay using (2):

$$U_i = \frac{(E_{s1} - E_{h1}) - (E_{s2} - E_{h2})}{A_{h1} - A_{h2}} \quad (2)$$

Where U_i = interval uplift rate; E_s= elevation of shoreline angle; E_h = paleo-highstand elevation; A_h = highstand age; and, 1 and 2 refer to the older and younger terrace platforms respectively. E_s and E_h are both relative to present-day sea level.

5.3 Long-term Uplift Rates and Differential Uplift across Yaquina Bay

5.3.1 Average Uplift Rates

Using the height for each paleoshoreline angle (Table 2) we calculated average coastal uplift rates (from the paleo-sea level highstand time to the present) for the terraces north of Yaquina Bay of 0.7 ± 0.1 m/kyr, 0.9 ± 0.1 m/kyr, and 0.7 ± 0.1 m/kyr for the MIS 5e, 5c and 5a terrace platforms respectively (Table 3). These values are at the higher end of previous uplift rate estimates of 0.5-0.8 m/kyr in this location (Kelsey et al., 1996). South of the bay, average uplift rates from the same terrace sequence are significantly lower at 0.3-0.4 m/kyr for all terrace platforms (Table 3, Figure 7). Our uplift rate estimates from terraces south of Yaquina Bay are consistent with those determined by Kelsey et al., (1996) (0.1-0.4 m/kyr). The average uplift rates since the late Pleistocene north of Yaquina Bay are approximately two times the average uplift rates south of Yaquina Bay. This differential uplift across Yaquina Bay is indicative of faulting within the bay (along the Yaquina Bay fault) at an average vertical slip rate of 0.5 ± 0.1 m/kyr (Figure 7).

5.3.2 Interval Uplift Rates

The elevation differences between the MIS 5e and MIS 5c (125-106 ka) terraces north and south of Yaquina Bay are primarily a result of differences in the highstand elevations. There is little additional uplift between MIS 5e and MIS 5c, yielding uplift rates that are near zero (-0.1 ± 0.7 m/kyr and 0.1 ± 0.8 m/kyr north and south of the bay respectively (Table 3, Figure 7)). However, between MIS 5c and MIS 5a (106-84 ka), uplift rates increase to 1.6 ± 0.6 m/kyr north of, and 0.2 ± 0.6 m/kyr south of the bay (Table 3, Figure 7), implying a vertical slip rate of ~1.4 ± 0.8 m/kyr along the Yaquina Bay fault during this time interval. From MIS 5a (84 ka) to the present uplift rates are 0.7 ± 0.1 m/kyr north, and 0.4 ± 0.1 m/kyr south of the bay (Table 3, Figure 7), implying a lower, but still significant, vertical slip rate of 0.3 ± 0.1 m/kyr along the Yaquina Bay fault over the last ~84 kyrs.

Table 3: Average Uplift Rates and Interval Uplift rates north and south of Yaquina Bay

Assigned Age (A_h) (ka)	Paleo-shoreline height (E_s) (m)	High-stand elevation (E_h) (m)	Surface uplift (m)	Uplift rate to present (m/kyr)	Surface uplift during interval (m)	Time Interval (kyrs)	Interval uplift rate (U_i) (m/kyr)
North of Bay							
Surface 1n (MIS 5a)							
84	45 ± 7	-15 ± 5	60 ± 9	0.7 ± 0.1	60 ± 8 (Interval=0-84 ka)	84	0.7 ± 0.1
Surface 2n (MIS 5c)							
106	86 ± 8	-9 ± 5	95 ± 9	0.9 ± 0.1	35 ± 13 (Interval=84-106 ka)	22	1.6 ± 0.6
Surface 3n (MIS 5e)							
125	103 ± 3	+9.5 ± 8.5	93.5 ± 9	0.7 ± 0.1	-1.5 ± 13 (Interval=106-125 ka)	19	-0.1 ± 0.7
South of Bay							
Surface 1s (MIS 5a)							
84	15 ± 7	-15 ± 5	30 ± 8	0.4 ± 0.1	30 ± 8 (Interval=0-84 ka)	84	0.4 ± 0.1
Surface 2s (MIS 5c)							
106	26 ± 9	-9 ± 5	35 ± 10	0.3 ± 0.1	5 ± 13 (Interval=84-106 ka)	22	0.2 ± 0.6
Surface 3s (MIS 5e)							
125	46 ± 9	+9.5 ± 8.5	36.5 ± 12	0.3 ± 0.1	1.5 ± 16 (Interval=106-125 ka)	19	0.1 ± 0.8
Errors reported for uplift rates incorporate errors in shoreline angle elevation, cover sediment thickness and paleo-sealevel highstand elevation.							

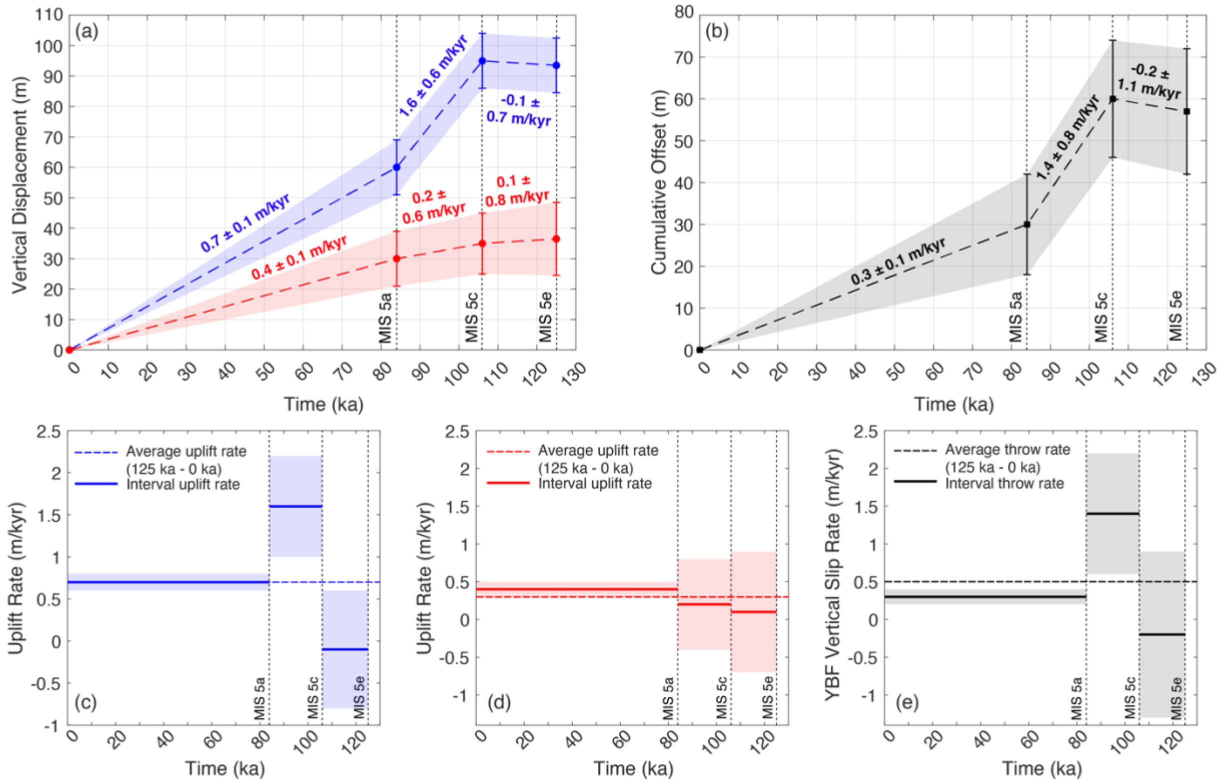

Figure 7: (a) Vertical displacement over the last 125 kyrs. Vertical displacement rates during each time interval are given by the slope of the line. (a)-(b) The shaded region shows the range of vertical displacements for each interval (see Table 3). Blue = north of Yaquina Bay, red = south of Yaquina Bay. (b) Cumulative vertical fault offset over the last 125 kyrs. The slope of the line gives the vertical slip rate over time. (c) Crustal uplift rates through time north of Yaquina Bay. (d) Crustal uplift rates through time south of Yaquina Bay. (e) Differential Uplift (associated with vertical slip along the Yaquina Bay fault (YBF)). (c)-(e) The shaded regions show the error associated with the crustal uplift and slip rates for each time interval (see Table 3). (a)-(e) Dashed black lines indicate the timing of MIS 5e, MIS 5c and MIS 5a.

6. Discussion

6.1 Faulting at Yaquina Bay

The north-side-up offset of the observed MIS 5 terraces across Yaquina Bay (Figures 6 and 7) requires slip since the late Pleistocene on the Yaquina Bay fault, as inferred by Kelsey et al. (1996). Because the MIS 5e and MIS 5c terraces are offset by approximately the same amount (~55-60 m) across Yaquina Bay, this suggests that there was little to no fault movement between

125 ka to 106 ka. This is consistent with the uplift rate results for this time interval (Table 3, Figure 7), which suggest the majority of the separation between these terraces (MIS 5e and MIS 5c) was due to changes in eustatic sea level with little additional uplift related to tectonic activity (Figure 7). In contrast, the MIS 5a terrace is displaced vertically by ~30 m and the MIS 5c terrace is displaced vertically by ~60 m across the bay (Figure 6, Table 3), implying differential motion of at least 0.6 ± 0.1 m/kyr on the Yaquina Bay fault since MIS 5c (~106 ka), in agreement with average throw rates for the fault estimated by Kelsey et al. (1996). Although the long-term displacement rate from MIS 5c to present is 0.6 ± 0.1 m/kyr, the differences in terrace elevation require greater throw rates (1.4 ± 0.8 m/kyr) in the time interval between 106 – 84 ka, reduced throw rates (0.3 ± 0.1 m/kyr) from 84 ka to present, and little to no displacement between 125 – 106 ka (Figure 7). Our results confirm that the Yaquina Bay fault has been active during the late Pleistocene, and it also appears that the fault has experienced significant variations in displacement over the last 125 kyrs, and that a significant amount of displacement accrued during a relatively short time period post-106 ka.

6.2 Variable Uplift and Slip Rates at Yaquina Bay

Sea level was ~18 m higher during MIS 5e compared to MIS 5c, and the MIS 5e and the MIS 5c paleo-shorelines are separated by ~17 m and 20 m north and south of the bay respectively (Table 3). Thus, most of the separation between the MIS 5e and MIS 5c terraces can be explained by sea level changes. The uplift rates of -0.1 ± 0.7 m/kyr and 0.1 ± 0.8 m/kyr calculated during this time interval (Table 3, Figure 7) are similar, within error, to other long-term uplift rates calculated along the Cascadia subduction zone, away from active upper-plate structures (e.g., Kelsey et al., 1994) (Figure 8). This suggests that the uplift over this time interval may be reflective of broader-scale uplift processes across the Cascadia margin, and not solely from local faulting at Yaquina Bay. Following MIS 5c, however, uplift north of Yaquina Bay was significantly higher in the ~20 kyr period between MIS 5c and MIS 5a – increasing from -0.1 ± 0.7 m/kyr to 1.6 ± 0.6 m/kyr (Figure 7). This is consistent with a differential uplift rate of ~1.4 m/kyr across the bay during this time interval, suggestive of relatively rapid slip along the Yaquina Bay fault between 106 ka to 84 ka. The MIS 5a to present time interval is 84 kyrs and significantly longer than the ~20 kyr intervals between MIS 5e and 5c and MIS 5c and 5a. Since we find highly variable uplift rates over time intervals of ~20 kyrs prior to 84 ka, it is possible that the uplift rate and thus slip rate on the Yaquina Bay fault has also varied significantly over the last 84 kyr, but no records (i.e., younger terraces) of this are preserved in this location.

6.3 Other Examples of Variable Uplift Along the Cascadia Margin and Beyond

Time-variable uplift also appears to characterize some terrace records in southern Cascadia, in the vicinity of Cape Ferrelo. Here, Kelsey and Bockheim (1994) determined long-term uplift rates for MIS 5a, 5c and 5e terraces exposed along a coastal segment between the Whaleshead fault zone and Chetco River Fault. Using equation (2), interval-specific uplift rates here (Table S5) appear to require an increase in uplift post-MIS 5c; the separation between the MIS 5c and MIS 5e terraces can be accounted for solely by changes in eustatic sea level (within the uncertainty of ± 6, reflecting both paleo-sea level highstand and elevation uncertainties). This implies there was little to no coastal uplift between MIS 5e and 5c in this location. The post-MIS 5c increase in uplift rate observed at Yaquina Bay and Cape Ferrelo may suggest an increase in fault slip rate along upper-plate faults in these regions, separated by ~300 km along the Cascadia margin. Although speculative, if these reflect coordinated changes in slip rate along upper-plate structures, there may be a broader-scale tectonic driver responsible for this increase in fault slip rates.

Variable uplift along the Oregon coast has also been interpreted at Cape Blanco (Kelsey, 1990). In this case, active anticlinal folding, has led to the uplift and preservation of MIS 5a, 5c, 5e and older terraces above present-day sea level. Here, a terrace platform contains marine sediment associated with three distinct sea level highstand periods (MIS 5e, 5c and 5a). Kelsey (1990) concluded that for this terrace geometry to be preserved, variable uplift over the last 125 kyrs is required, with an increase in uplift post-MIS 5c.

Variable uplift of marine terraces has also been documented in other subduction locations globally. For example, Yildirim et al. (2013) ascribed non-steady uplift since ca. 570 ka at the Sinop Peninsula, northern margin of the Central Anatolian Plateau, to a temporally variable faulting history in the region. Additionally, Saillard et al. (2009), document time-varying uplift

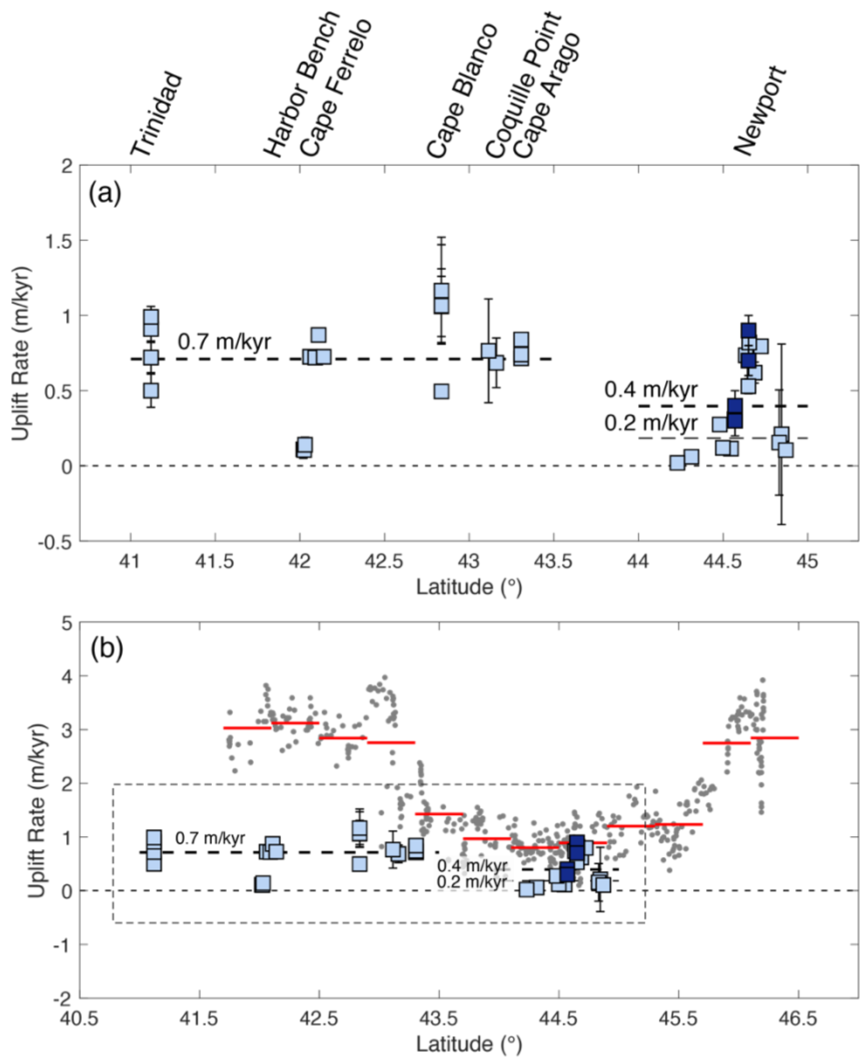

Figure 8: Geodetic and long-term uplift rates along the Cascadia margin. (a) Marine terrace uplift rates (light blue) along the Cascadia margin (Kelsey and Bockheim, 1994; Padgett et al., 2019; Kelsey, 1990; McInelly and Kelsey, 1990; Muhs et al, 1990; Kelsey et al., 1996; this study). The dark blue squares are the uplift rates from this study. Dashed lines show the average uplift rates from 41 °N to 43.5 °N and 44 °N to 45 °N. North of 44 °N the lower dashed line shows the average uplift excluding data north of Yaquina Bay where a coastal structural block from 44.6 °N to 44.8 °N has uplift rates > 0.5 m/kyr. (b) Compilation bench mark leveling uplift rates (grey circles, Burgette et al., 2009) and long-term coastal uplift rates from marine terraces (shown in (a)). The black box is the location of (a). Dashed lines through the marine terrace data are the same as in (a). The horizontal solid red lines through the geodetic data show the average geodetic uplift rate value over 0.4° latitudinal intervals.

rates along the Chilean margin, and suggest broader transient subduction-related processes, such as subduction erosion and/or sediment underplating, are responsible for this variable uplift.

6.4 Long-term versus Geodetic Uplift

Present-day coastal geodetic uplift rates derived from tidal and leveling data from ~43.5 °N – 46 °N are relatively low, typically < 1.5 m/kyr. In comparison coastal geodetic uplift rates further south (~41.5 °N – 43.5 °N) are on average ~3 m/kyr (Figure 8) (Burgette et al., 2009). Elevated geodetic uplift rates in southern Cascadia have been attributed to a variety of tectonic processes, including transitions in upper-plate strength (McKenzie et al., 2022), sediment underplating (Delph et al., 2021), and aestheospheric buoyancy (Bodmer et al., 2020). Similarly, long-term uplift rates from marine terrace platforms are slightly higher between 41°N – 43.5 °N (~0.7 m/kyr) than father north from ~43.5 °N – 45 °N (~0.4 m/kyr) (Kelsey et al., 1994) (Figure 8). However, these long-term uplift rates of 0.7 m/kyr and 0.4 m/kyr likely encompass variations in uplift rate associated with Quaternary faulting. For example, excluding the high uplift rates in the fault-bounded block from 44.6°N to 44.8°N (north of Yaquina Bay) implies that the average uplift rate from ~43.5 °N – 45 °N would have been ~0.1 – 0.2 m/kyr (Figure 8). Similarly, south of 43.5 °N the average long-term uplift rate decreases to ~0.2 – 0.3 m/kyr when the effects of faulting are removed, as shown in Kelsey et al. (1994). This uplift (away from upper-plate structures) comprises ~10-20% and ~5-10% of the geodetic signal in central (~43.5 °N – 45 °N) and southern (~41.5 °N – 43.5 °N) Cascadia respectively (Figure 8). This suggests a relatively large, and measurable, fraction of the uplift recorded geodetically (over 10s years) is maintained in the geologic record and recorded by the long-term (100,000-to-200,000 year) uplift of marine terrace platforms.

The relative role that upper-plate faults (such as the Yaquina Bay fault) play in generating variations in long-term coastal uplift is still an open question, and in Cascadia, the marine terraces documented in the literature are situated on prominent headlands that host higher than average uplift rates. For example, Point St. George in the hanging wall of the Saint George fault (Polenz and Kelsey, 1999), Trinidad headlands coastal reach (Padgett et al., 2019), Cape Ferrelo, (Kelsey and Bockheim, 1994), Cape Blanco (Kelsey, 1990), Cape Arago (McInelly and Kelsey, 1990, and the uplifted coastal block bounded by the Yaquina Bay fault on the south and the Cape Foulweather fault on the north (Kelsey et al., 1996) are all situated on blocks bound by upper-plate faults. Observations from recent megathrust earthquakes suggest that displacement along such upper-plate structures may be linked to co-seismic slip on the subduction megathrust (Bai et al., 2017; Duputel and Rivera, 2017; Furlong and Herman, 2017). For example, co-seismic slip on upper-plate faults has been observed prior to (foreshocks), following (aftershocks) and coincident with megathrust ruptures across subduction zones globally including the 2011 Mw 7.1 Aracaunia megathrust event in Chile (Hicks and Rietbrock, 2015); the 2014 Mw 8.1 Pisagua megathrust event in southern Peru-northern Chile (González et al., 2015), and the 2016 Mw 7.8 Kaikoura megathrust event in New Zealand (Furlong and Herman, 2017). Many of these upper-plate faults are thought to extend to the subduction interface, and in the Kaikoura case, experienced high amounts of slip (exceeding 10 m in places) (Hamling et al., 2017; Furlong and Herman, 2017; Wang et al., 2018). Additionally, during the Kaikoura event 0.6 m – 4.8 m of coastal uplift was recorded within several upper-plate fault-bounded blocks (Hamling et al., 2017). These observations across subduction zones globally highlight the role of co-seismic upper-plate faulting in generating uplift of fault-bounded blocks along the coastline. However, how these faults behave inter-seismically and how other subduction processes (subduction coupling, post-seismic deformation etc.) generate long-term deformation and contribute to coastal uplift remains poorly understood. We have shown that improved records of marine terrace ages have the potential to start to place constrains on the accumulation of subduction zone upper-plate permanent strain.

7. Conclusions

We present the first OSL and IRSL ages for marine terrace sand deposits along the Cascadia margin. These ages, in conjunction with our mapping of terrace surfaces show that each of the three MIS 5 marine terraces (5a, 5c and 5e) are exposed at either side of the bay. These terraces have been offset by up to ~60 m across the bay, requiring the presence of an active trench-perpendicular fault within Yaquina Bay, as previously proposed by Kelsey et al. (1996). The relative height of paleoshoreline angles associated with these terrace platforms suggest that this fault accommodates time-variable displacement of the northern block, relative to the southern block, over the past ~125ka. In particular, the uplift rate north of Yaquina Bay between 84-106 ka is 1.6 m/kyr, significantly higher than the uplift rate south of Yaquina Bay during this time interval (0.2 m/kyr). This difference in uplift rate across Yaquina Bay implies that the throw rate along the Yaquina Bay fault exceeded ~1 m/kyr during this period (84-106 ka), likely reflecting a series of large-displacement events clustered along this upper-plate fault.

Acknowledgements

This work was funded under National Science Foundation Grants EAR-1758463 (awarded to EK) and EAR-1757581 (awarded to KPF). The geochronology analyses were funded by an AGeS2 research grant awarded to KAM (based upon work supported by the National Science Foundation under Grants EAR-1759200 and EAR-1759353).

We thank Katherine Worms for providing field assistance during sample collection and those at the Utah State University Luminescence Laboratory for their help in sample preparation and analyses. We thank Schmitty Thompson and Jessica Creveling for providing us with a GIA-corrected (modeled) MIS 5e highstand value for Newport, OR. We thank the editor and two anonymous reviewers for their comments, that have helped us in improving the manuscript.

References

Adams, J. (1984). Active Deformation of the Pacific Northwest Continental Margin. Tectonics, 3(4), 449-472

Aitken, M.J. (1998). An Introduction to Optical Dating: The dating of Quaternary sediments by the Use of photon-stimulated luminescence. Oxford University Press, Oxford, New York, Tokyo. https://doi.org/10.1017/S0016756899551777

Aitken, M.J., Xie, J. (1990). Moisture correction for annual gamma dose. Ancient TL, 8(2), 6-9

Atwater, B.F. (1987) Evidence for Great Holocene Earthquakes Along the Outer Coast of Washington State. Science, 236(4804), 942-944. https://doi.org/10.1126/science.236.4804.942

Atwater, B.F., Hemphill-Haley, E. (1997). Recurrence Intervals for Great Earthquakes of the Past 3,500 Years at Northeastern Willapa Bay, Washington. *U.S. Geological Survey Professional Paper 1576.* https://doi.org/10.3133/pp1576

Atwater, B.F., Stuiver, M., Yamaguchi, D.K. (1991). Radiocarbon test of earthquake magnitude at the Cascadia subduction zone. Nature, 353, 156-158. https://doi.org/10.1038/353156a0

Auclair, M., Lamothe, M., Huot, S. (2003). Measurement of anomalous fading for feldspar IRSL using SAR. Radiation Measurements, 37(405), 487-492. https://doi.org/10.1016/S1350-4487(03)00018-0

Bai, Y., Lay, T.L., Cheung, K.F., Ye, L. (2017). Two regions of seafloor deformation generated the tsunami for the 13 November 2016, Kaikoura, New Zealand earthquake. Geophysical Research Letters, 44(13), 6597-6606. https://doi.org/10.1002/2017GL073717

Bloom, A.L., Broecker, W.S., Chappell, J.M.A., Matthews, R.K., Mesolella, K.J. (1974). Quaternary Sea Level Fluctuations on a Tectonic coast: New $^{230}Th/^{234}U$ Dates from the Huon Peninsula, New Guinea. Quaternary Research, 4(2), 185-205. https://doi.org/10.1016/0033-5894(74)90007-6

Bradley, W.C., Griggs, G.B. (1976). Form, genesis, and deformation of central California wave-cut platforms. GSA Bulletin, 87(3), 433-449. https://doi.org/10.1130/0016-7606(1976)87<433:FGADOC>2.0.CO;2

Bodmer, M., Toomey, D.R., VanderBeek, B., Hooft, E.E., Byrnes, J.S. (2020). Body Wave Tomography of the Cascadia Subduction Zone and Juan de Fuca Plate System: Identifying Challenges and Solutions for Shore-Crossing Data. Geochemistry, Geophysics, Geosystems, 21(12). https://doi.org/10.1029/2020GC009316

Bowles, C.J., Cowgill, E. (2012). Discovering marine terraces using airborne LiDAR along the Mendocino-Sonoma coast, northern California. Geosphere, 8(2), 386-402. https://doi.org/10.1130/GEOS00702.1

Burgette, R.J., Weldon II, R.J., Schmidt, D.A. (2009). Interseismic uplift rates for western Oregon and along-strike variation in locking on the Cascadia subduction zone. Journal of Geophysical Research: Solid Earth, 114 (B1), 1-24. https://doi.org/10.1029/2008JB005679

Clague, J.J., Bobrowsky, P.T., Hutchinson, I. (2000). A review of geological records of large tsunamis at Vancouver Island, British Columbia, and implications for hazard. Quaternary Science Reviews, 19, 849-863. https://doi.org/10.1016/S0277-3791(99)00101-8

Chappell, J. Shackleton, N.J. (1986). Oxygen isotopes and sea level. Nature, 324, 137-140. https://doi.org/10.1038/324137a0

Creveling, J.R., Mitrovica, J.X., Hay, C.C., Austermann, J., Kopp, R.E. (2015). Revisiting tectonic corrections applied to Pleistocene sea-level highstands. Quaternary Science Reviews, 111, 72-80. https://doi.org/10.1016/j.quascirev.2015.01.003

Creveling, J.R., Mitrovica, J.X., Clark, P.U., Waelbroeck, C., Pico, T. (2017). Predicted bounds on peak global mean sea level during marine isotope stage 5a and 5c. Quaternary Science Reviews, 163, 193-208. https://doi.org/10.1016/j.quascirev.2017.03.003

Delph J.R., Thomas A.M., Levander A. (2021). Subcretionary tectonics: Linking variability in the expression of subduction along the Cascadia forearc. EPSL, 556, 116724 https://doi.org/10.1016/j.epsl.2020.116724

Duputel, Z., Rivera, L. (2017). Long-period analysis of the 2016 Kaikoura earthquake. Physics of the Earth and Planetary Interiors, 265, 62-66. https://doi.org/10.1016/j.pepi.2017.02.004

Frankel, K.L., Dolan, J.F. (2007). Characterizing arid region alluvial fan surface roughness with airborne laser swath mapping digital topographic data. JGR: Earth Surface, 112(F02025). https://doi.org/10.1029/2006JF000644

Furlong, K.P., Herman, M. (2017). Reconciling the deformational dichotomy of the 2016 M_w 7.8 Kaikoura New Zealand earthquake. Geophysical Research Letters, 44(13), 6788-6791. https://doi.org/10.1002/2017GL074365

Galbraith, R.F., Roberts, R.G. (2012). Statistical aspects of equivalent dose and error calculation and display in OSL dating: An overview and some recommendations. Quaternary Geochronology, 11, 1-27. https://doi.org/10.1016/j.quageo.2012.04.020

Gallen, S.F., Wegmann, K.W., Bohnenstiehl, D.R., Pazzaglia, F.J., Brandon, M.T., Fassoulas, C. (2014). Active simultaneous uplift and margin-normal extension in a forearc high, Crete, Greece. Earth and Planetary Science Letters, 398, 11-24. https://doi.org/10.1016/j.epsl.2014.04.038

Goldfinger, C., Nelson, C.H., Morey, A.E., Johnson, J.E., Patton, J.R., Karabanov, E.B., Gutiérrez-Pastor, J., Eriksson, A.T., Gracia, E., Dunhill, G., Enkin, R.J., Dallimore, A., Vallier, T. (2012). Turbidite event history – Methods and implications of Holocene paleoseismicity of the Cascadia subduction zones: *U.S. Geological Survey Professional Paper* 1661-F, 170 p. https://doi.org/10.3133/pp1661F

González, G., Salazar, P., Loveless, J.P., Allmendinger, R.W., Aron, F., Shrivastava, M. (2015). Upper plate reverse fault reactivation and the unclamping of the megathrust during the 2014 northern Chile earthquake sequence. Geology, 43(8), 671-674. https://doi.org/10.1130/G36703.1

Govers, R., Furlong, K.P., van de Wiel, L., Herman, M.W., Broerse, T. (2017). The Geodetic Signature of the Earthquake Cycle at Subduction Zones: Model Constraints on the Deep Processes. Reviews of Geophysics, 56(1), 6-49. https://doi.org/10.1002/2017RG000586

Griggs, A.B. (1945). Chromite-bearing sands of the southern part of the coast of Oregon. USGS Bulletin 945-E. https://doi.org/10.3133/b945E

Guérin, G., Mercier, N., Adamiec, G. (2011). Dose-rate conversion factors: update. Ancient TL, 29, 5-8

Hamling, I.J., Hreinsdóttir, S., Clark, K., Elliott, J., Liang C., Fielding, E., Litchfield, N., Villamor, P., Wallace, L., Wright, T.J., D'Anastasio E., Bannister, S., Burbidge, D., Denys, P., Gentle, P., Howarth, J., Mueller, C., Palmer, N., Pearson, C., Power, W., Barnes, P., Barrell, D.J.A., Van Dissen, R., Langridge, R., Little, T., Nicol, A., Pettinga, J., Rowland, J., Stirling, M. (2017). Complex multifault rupture during the 2016 Mw 7.8 Kaikōura earthquake, New Zealand, Science, 356(6334). https://doi.org/10.1126/science.aam7194

Hawkes, A.D., Horton, B.P., Nelson, A.R., Vane, C.H., Sawai, Y. (2011). Coastal subsidence in Oregon, USA, during the giant Cascadia earthquake of AD 1700, Quaternary Science Reviews, 30(3-4), 364-376. https://doi.org/10.1016/j.quascirev.2010.11.017

Hayes, G. (2018). Slab2 - A Comprehensive Subduction Zone Geometry Model. U.S. Geological Survey data release. https://doi.org/10.5066/F7PV6JNV

Hicks, S.P., Rietbrock, A. (2015). Seismic slip on an upper-plate normal fault during a large subduction megathrust rupture. Nature, 8, 955-960. https://doi.org/10.1038/ngeo2585

Huntley, D.J., Baril, M.R. (1997). The K content of the K-feldspars being measured in optical dating or in thermoluminescence dating. Ancient TL, 15(1), 11-13

Huntley, D.J., Hancock, R.G.V. (2001). The Rb contents of the K-feldspar grains being measured in optical dating. Ancient TL, 19(2), 43-46

Huntley, D.J., Lamothe, M. (2001). Ubiquity of anomalous fading in K-feldspars and correction for it in optical dating. Canadian Journal of Earth Sciences, 38(7). https://doi.org/10.1149/e01-013

Hsu, J.T. (1992). Quaternary uplift of the peruvian coast related to subduction of the Nazca Ridge: 13.5 to 15.6 degrees south latitude. Quaternary International, 15-16, 87-97. https://doi.org/10.1016/1040-6182(92)90038-4

Jacobs, Z. (2008). Luminescence chronologies for coastal and marine sediments. Boreas, 37(4), 508-535. https://doi.org/10.1111/j.1502-3885.2008.00054.x

Kelsey, H.M. (1990). Late Quaternary Deformation of Marine Terraces on the Cascadia Subduction Zone near Cape Blanco, Oregon. Tectonics, 9(5), 983-1014. https://doi.org/10.1029/TC009i005p00983

Kelsey, H.M., Bockheim, J.G. (1994). Coastal landscape evolution as a function of eustasy and surface uplift rate, Cascadia margin, southern Oregon. GSA Bulletin, 106(6), 840-854. https://doi.org/10.1130/0016-7606(1994)106<0840:CLEAAF>2.3.CO;2

Kelsey, H.M., Engebretson, D.C., Mitchell, C.E., Ticknor, R.L. (1994). Topographic Form of the Coast Ranges of the Cascadia margin in relation to coastal uplift rates and plate subduction. Journal of Geophysical Research, 99(B6), 12245-12255. https://doi.org/10.1029/93JB03236

Kelsey, H.M., Ticknor, R.L., Bockheim, J.G., Mitchell, C.E. (1996). Quaternary upper plate deformation in coastal Oregon. GSA Bulletin, 108(7), 843-860. https://doi.org/10.1130/0016-7606(1996)108<0843:QUPDIC>2.3.CO;2

Kelsey, H.M., Witter, R.C., Hemphill-Haley, E., (2002). Plate-boundary earthquakes and tsunamis of the past 5500 yr, Sixes River estuary, southern Oregon. GSA Bulletin, 114(3), 298-314. https://doi.org/10.1130/0016-7606(2002)114<0298:PBEATO>2.0.CO;2

Kelsey, H.M., Nelson, A.R., Hemphill-Haley, E., Witter, R.C. (2005). Tsunami history of an Oregon coastal lake reveals a 4600 yr record of great earthquakes on the Cascadia subduction zone. GSA Bulletin, 117(7-8), 1009-1032. https://doi.org/10.1130/B25452.1

Kennedy, G.L., Lajoie, K.R., Wehmiller, J.F. (1982). Aminostratigraphy and faunal correlations of late Quaternary marine terraces, Pacific Coast, USA. Nature, 299, 545-547. https://doi.org/10.1038/299545a0

Kobor, J.S., Roering, J.J. (2004). Systematic variation of bedrock channel gradients in the central Oregon Coast Range: implications for rock uplift and shallow landsliding. Geomorphology, 62(304), 239-256. https://doi.org/10.1016/j.geomorph.2004.02.013

Lajoie, K.R. (1986). Coastal tectonics *in* Active tectonics: Washington, D.C., National Academy Press, p. 95-124.

Ludwin, R.S., Dennis, R., Carver, D., McMillan, A.D., Losey, R., Clague, J., Jonientz-Trisler, C., Bowechop, J., Wray, J., James, K. (2005) Dating the 1700 Cascadia Earthquake: Great Coastal Earthquake in Native Stories. *Seismological Research Letters*, 76(2), 140-184. https://doi.org/10.1785/gssrl.76.2.140

Madsen, A.T. and Murray, A.S., 2009. Optically stimulated luminescence dating of young sediments: A review. Geomorphology, 109(1-2), 3-16. https://doi.org/10.1016/j.geomorph.2008.08.020

Matsu'ura, T. (2015). Late Quaternary uplift rate inferred from marine terraces, Muroto Peninsula, southwest Japan: Forearc deformation in an oblique subduction zone. *Geomorphology*, 234, 133-150. https://doi.org/10.1016/j.geomorph.2015.01.012

Mejdahl, V. (1979). Thermoluminescence dating: Beta-dose attenuation in quartz grains. Archaeometry, 21, 61-72. https://doi.org/10.1111/j.1475-4754.1979.tb00241.x

Melnick, D., Bookhagen, B., Echtler, J.P., Strecker, M.R. (2006). Coastal deformation and great subduction earthquakes, Isla Santa María, Chile (37°S). GSA Bulletin, 118(11-12), 1463-1480. https://doi.org/10.1130/B25865.1

Meltzner, A.J., Sieh, K., Abrams, M., Agnew, D.C., Hudnut, K.W., Avouac, J-P., Natawidaja, D.H. (2006). Uplift and subsidence associated with the great Aceh-Andaman earthquake of 2004. JGR: Solid Earth, 111(B2). https://doi.org/10.1029/2005JB003891

Merritts, D., Bull, W.B. (1989). Interpreting Quaternary uplift rates at the Mendocino triple junction, northern California, from uplifted marine terraces. Geology, 17(11), 1020-1024. https://doi.org/10.1130/0091-7613(1989)017<1020:IQURAT>2.3.CO;2

McInelly, G.W., Kelsey, H.M. (1990). Late Quaternary Tectonic Deformation in the Cape Arago-Bandon Region of Coastal Oregon as Deduced From Wave-Cut Platforms. JGR: Solid Earth, 95(B5), 6699-6713. https://doi.org/10.1029/JB095iB05p06699

McKenzie, K.A., Furlong, K.P., Herman, M.W. (2022). Regional and Local Patterns of Upper-Plate Deformation in Cascadia: The Importance of the Down-Dip Extent of Locking

Relative to Upper-Plate Strength Contrasts. Tectonics, 41(1). https://doi.org/10.1029/2021TC007062

McNeill, L.C., Goldfinger, C., Kulm, L.D., Yeats, R.S. (2000). Tectonics of the Neogene Cascadia forearc basin: Investigations of a deformed late Miocene unconformity. GSA Bulletin, 112(8), 1209-1224. https://doi.org/10.1130/0016-7606(2000)112<1209:TOTNCF>2.0.CO;2

Morel, D.L., Morell, K.D., Keller, E.A., Rittenour, T.M. (2022). Quaternary chronology and rock uplift recorded by marine terraces, Gaviota coast, Santa Barbara County, California, USA. GSA Bulletin, 134(3/4), 871-884. https://doi.org/10.1130/B35609.1

Muhs, D.R. (2022). MIS 5e sea-level history along the Pacific coast of North America. Earth Syst. Sci. Data, 14, 1271-1330. https://doi.org/10.5194/essd-14-1271-2022

Muhs, D.R., Kelsey, H.M., Miller, G.H., Kennedy, G.L., Whelan, J.F. (1990). Age Estimates and Uplift Rates for Late Pleistocene Marine Terraces: Southern Oregon Portion of the Cascadia Forearc. JGR: Solid Earth, 95(B5), 6685-6698. https://doi.org/10.1029/JB095iB05p06685

Muhs, D.R. (1992). The last interglacial-glacial transition in North America: Evidence from uranium-series dating of coastal deposits. In Clark, P.U. and Lea, P.D. (eds), The Last Interglacial-Glacial Transition in North America. Geological Society of America Special Paper 270, 31-51. https://doi.org/10.1130/SPE270-p31

Muhs, D.R., Rockwell, T.K., Kennedy, G.L. (1992). Late quaternary uplift rates of marine terraces on the Pacific coast of North America, southern Oregon to Baja California sur. Quaternary International, 15-16, 121-133. https://doi.org/10.1016/1040-6182(92)90041-Y

Muhs, D.R., Schumann, R.R., Groves, L.T., Simmons, K.R., Florian, C.R. (2021). The marine terraces of Santa Cruz Island, California: Implications for glacial isostatic adjustment models of last-interglacial sea-level history. Geomorphology, 389, 107826. https://doi.org/10.1016/j.geomorph.2021.107826

Muhs, D.R., Schweig, E.S., Simmons, K.R. (2020). Late Quaternary sea-level history of Saipan, Commonwealth of Northern Mariana Islands, USA: A test of tectonic uplift and glacial isotatic adjustment models. GSA Bulletin, 132(3-4), 863-883. https://doi.org/10.1130/B35162.1

Muhs, D.R., Simmons, K.R., Kennedy, G.L., Ludwig, K.R., Groves, L.T. (2006). A cool eastern Pacific Ocean at the close of the Last Interglacial complex. Quaternary Science Reviews, 25(3-4), 235-262. https://doi.org/10.1016/j.quascirev.2005.03.014

Muhs, D.R., Simmons, K.R., Schumann, R.R., Groves, L.T., Mitrovica, J.X., Laurel, D. (2012). Sea-level history during the Last Interglacial complex on San Nicholas Island, California: implications for glacial isostatic adjustment processes, paleozoogeography and tectonics. Quaternary Science Reviews, 37, 1-25. https://doi.org/10.1016/j.quascirev.2012.01.010

Murray, A.S., Wintle, A.G. (2000). Luminescence dating of quartz using an improved single-aliquot regenerative-dose protocol. Radiation Measurements, 32(1), 57-73. https://doi.org/10.1016/S1350-4487(99)00253-X

Murray, A.S., Wintle, A.G. (2003). The single aliquot regenerative dose protocol: potential for improvements in reliability. Radiation Measurements, 37(4-5), 377-381. https://doi.org/10.1016/S1350-4487(03)00053-2

Nelson, A.R., Atwater, B.F., Bobrowsky, P.T., Bradley, L-A., Clague, J.J., Carver, G.A., Darienzo, M.E., Grant, W.C., Krueger, H.W., Sparks, R., Stafford Jr., T.W., Stuiver, M. (1995). Radiocarbon evidence for extensive plate-boundary rupture about 300 years ago at the Cascadia subduction zone. Nature, 378, 371-374. https://doi.org/10.1038/378371a0

Nelson, M.S., Rittenour, T.M., (2015). Using grain-size characteristics to model soil water content: application to dose-rate calculation for luminescence dating. Radiation Measurements, 81, 142-149. https://doi.org/10.1016/j.radmeas.2015.02.016

Nelson, A.R., Sawai, Y., Jennings, A.E., Bradley, L-A., Gerson, L., Sherrod, N.L., Sabean, J., Horton, B.P. (2008). Great-earthquake paleogeodesy and tsunamis of the past 2000 years at Alsea Bay, central Oregon coast, USA. Quaternary Science Reviews, 27(7-8), 747-768. https://doi.org/10.1016/j.quascirev.2008.01.001

Padgett, J.S., Kelsey, H.M., Lamphear, D. (2019). Upper-plate deformation of Late Pleistocene marine terraces in the Trinidad, California, coastal area, southern Cascadia subduction zone. Geosphere, 15(4), 1323-1341. https://doi.org/10.1130/GES02032.1

Polenz, M., Kelsey, H.M. (1999). Development of a Late Quaternary Marine Terraced Landscape during On-Going Tectonic Contraction, Crescent City Coastal Plain, California. Quaternary Research, 52(2), 217-228. https://doi.org/10.1006/qres.1999.2061

Prescott, J.R., Hutton, J.T. (1994). Cosmic ray contributions to dose rates for luminescence and ESR dating. Radiation Measurements, 37, 377-381. https://doi.org/10.1016/1350-4487(94)90086-8

Racano, S., Jara-Muñoz, J., Cosentino, D., Melnick, D. (2020). Variable Quaternary Uplift Along the Southern Margin of the Central Anatolian Plateau Inferred From Modeling Marine Terrace Sequences. Tectonics, 29(12). https://doi.org/10.1029/2019TC005921

Ramírez-Herrera, M.T., Gaidzik, K., Forman, S., Kostoglodov, V., Bürgmann, R., Johnson, C.W. (2018). Relating the long-term and short-term vertical deformation across a transect of the forearc in the central Mexican subduction zone. Geosphere, 14(2), 419 439. https://doi.org/10.1130/GES01446.1

Rees-Jones, J. (1995). Optical dating of young sediments using fine-grain quartz. Ancient TL, 14, 9-14

Saillard, M., Hall, S.R., Audin, L., Farber, D.L., Regard, V., Hérail, G. (2011). Andean coastal uplift and active tectonics in southern Peru: ^{10}Be surface exposure dating of differentially uplifted marine terrace sequences (San Juan de Marcona, ~ 15.4°S). Geomorphology, 128(3-4), 178-190. https://doi.org/10.1016/j.geomorph.2011.01.004

Saillard, M., Audin, L., Rousset, B., Avouac, J-P., Chlieh, M., Hall, S.R., Husson, L., Farber, D.L. (2017). From the seismic cycle to long-term deformation: linking seismic coupling and Quaternary coastal geomorphology along the Andean megathrust. Tectonics, 36(2), 241-256. https://doi.org/10.1002/2016TC004156

Saillard, M., Hall, S.R., Audin, L., Farber, D.L., Hérail, G., Martinod, J., Regard, V., Finkel, R.C., Bondoux, F. (2009). Non-steady long-term uplift rates and Pleistocene marine terrace development along the Andean margin of Chile (31°S) inferred from ^{10}Be dating. Earth and Planetary Science Letters, 277(1-2), 50-63. https://doi.org/10.1016/j.epsl.2008.09.039

Satake, K., Shimazaki, K., Tsuji, Y., Ueda, K. (1996). Time and size of a giant earthquake in Cascadia inferred from Japanese tsunami records of January 1700. Nature, 369, 246-249. https://doi.org/10.1038/379246a0

Shackleton, N.J., Opdyke, N.D. (1973). Oxygen Isotope and Palaeomagnetic Stratigraphy of Equatorial Pacific Core V28-238: Oxygen Isotope Temperatures and Ice Volumes on a

105 Year and 106 Year Scale. Quaternary Research, 3(1), 39-55. https://doi.org/10.1016/0033-5894(73)90052-5

Simms, A.R., Rouby, H., Lambeck, K. (2016). Marine terraces and rates of vertical tectonic motion: The importance of glacio-isostatic adjustment along the Pacific coast of central North America. GSA Bulletin, 128(1-2), 81-93. https://doi.org/10.1130/B31299.1

Snavely, P.D., Jr., MacLeod, N.S., Wagner, H.C., Rau, W.W. (1976). Geologic map of the Yaquina and Toledo quadrangles, Lincoln County, Oregon. Scale 1:62,500, Map I-867, U.S. Geological Survey. https://doi.org/10.3133/i867

Thackary, G.D. (1998). Convergent-margin deformation of Pleistocene strata on the Olympic coast of Washington, USA. In Stewart, I.S. and Vita-Finzi, C. (eds), Coastal Tectonics. Geological Society, London, Special Publications, 146, 199-211. https://doi.org/10.1144/GSL.SP.1999.146.01.11

VanLaningham, S., Meigs, A., Goldfinger, C. (2006). The effects of rock uplift and rock resistance on river morphology in a subduction zone forearc, Oregon, USA. Earth Surface Processes and Landforms, 31, 1257-1279. https://doi.org/10.1002/esp.1326

Victor, P., Sobiesiak, M., Glodny, J., Nielsen, N., Oncken, O. (2011). Long-term persistence of subduction earthquake segment boundaries: Evidence from Mejillones Peninsula, northern Chile, JGR: Solid Earth, 116(B2). https://doi.org/10.1029/2010JB007771

Wallinga, J., Murray, A., Wintle, A. (2000). The single-aliquot regenerative-dose (SAR) protocol applied to coarse-grain feldspar. Radiation Measurements, 32(5-6), 529-533. https://doi.org/10.1016/S1350-4487(00)00091-3

Wang, P-L., Engelhart, S.E., Wang, K., Hawkes, A.D., Horton, B.P., Nelson, A.R., Witter, R.C. (2013). Heterogeneous rupture in the great Cascadia earthquake of 1700 inferred from coastal subsidence estimates. JGR: Solid Earth, 118(5), 2460-2473. https://doi.org/10.1002/jgrb.50101

Wang, D., Chen, Y., Wang, Q., Mori, J. (2018). Complex rupture of the 13 November 2016 M_w 7.8 Kaikoura, New Zealand earthquake: Comparison of high-frequency and low-frequency observations.Tectonophysics, 733, 100-107. https://doi.org/10.1016/j.tecto.2018.02.004

West, D.O., McCrumb, D.R. (1988). Coastline uplift in Oregon and Washington and the nature of Cascadia subduction zone tectonics. Geology, 16(2), 169-172. https://doi.org/10.1130/0091-7613(1988)016<0169:CUIOAW>2.3.CO;2

Wintle, A.G., Murray, A.S. (2006). A review of quartz optically stimulated luminescence characteristics and their relevance in single-aliquot regeneration dating protocols. Radiation Measurements, 41(4), 369-391. https://doi.org/10.1016/j.radmeas.2005.11.001

Witter, R.C., Kelsey, H.M., Hemphill-Haley, E. (2003). Great Cascadia earthquakes and tsunamis of the past 6700 years, Coquille River estuary, southern coastal Oregon. GSA Bulletin, 115(10), 1289-1306. https://doi.org/10.1130/B25189.1

Witter, R.C., Zhang, Y., Wang, K., Goldfinger, C., Priest, G.R., Allan, J.C. (2012). Coseismic slip on the southern Cascadia megathrust implied by tsunami deposits in an Oregon lake and earthquake-triggered marine turbidites. JGR: Solid Earth, 117(B10). https://doi.org/10.1029/2012JB009404

Yamaguchi, D.K., Atwater, B.F., Bunker, D.E., Benson, B.E., Reid, M.S. (1997). Tree-ring dating the 1700 Cascadia earthquake. *Nature*, 389, 922-923. https://doi.org/10.1038/40048

Yildirim, C., Melnick, D., Ballato, P., Schildgen, T.F., Echtler, H., Erginal, A.E., Kıyak, N.G., Strecker, M.R. (2013). Differential uplift along the northern margin of the Central Anatolian Plateau: inferences from marine terraces. Quaternary Science Reviews, 81, 12-28. https://doi.org/10.1016/j.quascirev.2013.09.011